Journal of The
Electrochemical Society

OPEN ACCESS

A Mathematically Optimized Design Solution for Structure of PEMFC Catalyst Layer Based on a Two-Phase Flow Model

To cite this article: Mehrzad Alizadeh *et al* 2024 *J. Electrochem. Soc.* **171** 114506

Journal of The Electrochemical Society, 2024 **171** 114506

A Mathematically Optimized Design Solution for Structure of PEMFC Catalyst Layer Based on a Two-Phase Flow Model

Mehrzad Alizadeh,[1,z] Patcharawat Charoen-amornkitt,[2] Takahiro Suzuki,[1] and Shohji Tsushima[1]

[1]*Department of Mechanical Engineering, Graduate School of Engineering, Osaka University, Suita, 565-0871 Osaka, Japan*
[2]*Electrochemical Energy Storage and Conversion Laboratory, Department of Mechanical Engineering, Faculty of Engineering, King Mongkut's University of Technology Thonburi, Thung Khru, 10140, Bangkok, Thailand*

Proton exchange membrane fuel cells (PEMFCs) have emerged as a promising solution as the world is moving toward sustainable energy resources. However, in order to compete economically with existing technologies, further improvements in performance are necessary. Mathematical modeling and optimization are viable tools for designing better PEMFCs. This study aims to provide a framework for topological optimization of the electrode structure, with the ultimate goal of enhancing cell performance. To achieve this, a two-phase flow model of PEMFC is developed to characterize the cell performance. The model is then coupled with a topology optimization technique, which is the main focus of the present work, to seek an optimized constituent distribution in the catalyst layer. Results indicate that an electrode with a heterogeneous structure can enhance the overall cell performance by balancing various transport and rate processes. The optimized designs are investigated for various key factors, including effective diffusivity, effective conductivity, and liquid water management, to demonstrate how an optimized design can be advantageous.
 [DOI: 10.1149/1945-7111/ad8efe]

Manuscript submitted May 23, 2024; revised manuscript received October 4, 2024. Published November 13, 2024.

As the world is moving toward carbon-free energy resources, electrochemical energy conversion and storage technologies, such as secondary batteries and fuel cells, received much attention.[1,2] In particular, proton exchange membrane fuel cells (PEMFCs) have attracted significant attention due to their high efficiency, high power density, and low startup time, as well as their scalability and ability to operate at low temperatures. These characteristics make PEMFCs suitable for a wide range of applications, from stationary power generation[3,4] to transportation.[5,6] Although they offer various advantages, their manufacturing cost remains high due to the use of precious metals such as platinum as catalysts, which poses a significant obstacle to their widespread commercial adoption.[7–10] Therefore, it is crucial to focus on further enhancing their performance and reducing costs to make these energy devices more feasible for extensive deployment. This goal might be achieved by enhancement of a vital component called catalyst layer (CL), which is shown in Fig. 1a.

The significance of CL is twofold: (1) it is the largest cost contributor, and (2) the electrochemical reaction is taking place in this component. As previously mentioned, the former is attributed to the usage of costly noble metals as catalysts to increase the electrochemical reaction rate. CL is a crucial determinant of the overall performance of a PEMFC, as it facilitates several coupled transport phenomena, including mass and electric charge transfer, alongside electrochemical reactions. As a result, any improvement in CL not only reduces system costs but also enhances cell performance. The CL of a PEMFC is a thin, porous medium consisting of a catalyst supported by a support material (such as carbon-supported platinum), a polymeric binder material (ionomer), and voids. This triple-phase layer serves as the bed for redox reactions, where the fuel and oxidant undergo reduction and oxidation, respectively, on the catalyst material's surface. The electrochemical reaction involves chemical substances, electrons, and protons. In the CL, carbon-supported platinum (PtC) and ionomer phases are responsible for transporting electrons and protons, respectively. In addition, the reactant is delivered to the reaction site through the pores.

Several approaches have been attempted in previous research works to address the performance-cost challenge of CL. For instance, some studies explored the use of cheaper catalyst materials, such as non-platinum group metals, to reduce fabrication costs.[11–16] However, substituting platinum group metals (PGMs) with other elements in the fabrication of PGM-free catalyst layers can pose new challenges, such as low durability and reduced oxygen reduction reaction (ORR) activity. Thicker electrodes can be used to overcome the low ORR activity issue, but this can increase mass transport resistance and degrade liquid water discharge.[17] In another attempt, a number of studies[18–21] employed electroanalytical methods to assess and obtain a deeper understanding of electrode modification. Moreover, over the last three decades, remarkable dedication and substantial advancements have been devoted to improving PEMFCs performance by focusing on modeling of CL with the goal of optimizing its structure and composition.[22–31] A summary of some selected past research works on this topic is presented in Table I. Numerical methods are efficient approaches in designing superior CL and have been vastly used in the literature.[32–36] This strategy is based on mathematical modeling and optimization of CL structure. Mathematical modeling provides a powerful tool for simulation of cell characteristics under various structural and operational conditions. By changing any structural or operational parameter, the impacts of these changes might be determined. When integrated with mathematical optimization algorithms, the best set of parameters might be identified within a given bound.[37] As aforementioned, several coupled transport phenomena, including mass, heat, and electric charge transfer, and a rate process (i.e., electrochemical reaction) are happening simultaneously in CL. The cell performance is mainly dictated by two mechanisms in CL: (1) charge transfer rate, and (2) reactant supply/product discharge rate. Charge transfer rate represents how fast the reactant species are consumed (or likewise, product species are produced). On the other hand, the latter mechanism specifies the pace of reactant delivery to the reaction site (or product discharge from reaction site). This mechanism is also known as mass transport resistance and becomes dominant when a PEMFC is working at a high current density. At higher current densities, the rate of the chemical reaction increases, causing the reactant substance to be consumed more rapidly. To maintain the desired reaction rate, it is necessary to compensate the available amount of reactant accordingly. Insufficient reactant delivery leads to a substantial performance drop at high current densities. Moreover, excess liquid water production at these current density regions blocks the pores and makes the reactant delivery more complicated. This phenomenon is known as flooding.[38,39] In a

[z]E-mail: alizadeh.mehrzad@gmail.com

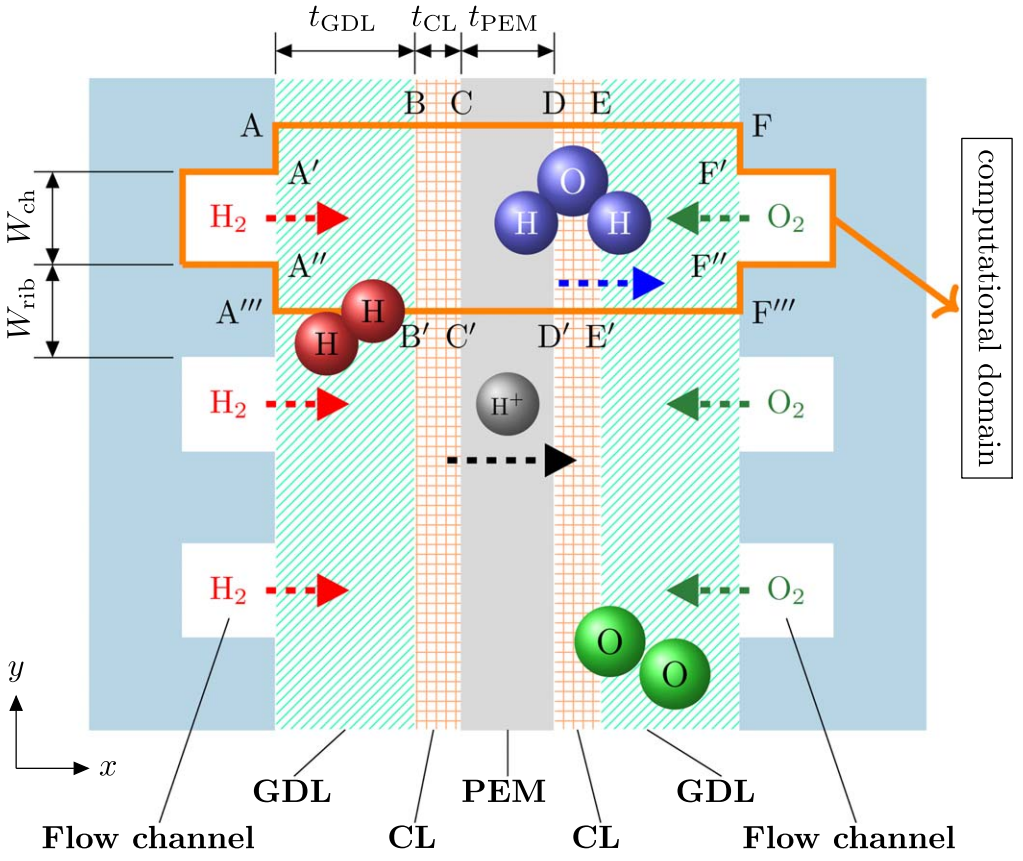

(a) 2D schematic diagram of a PEMFC cell

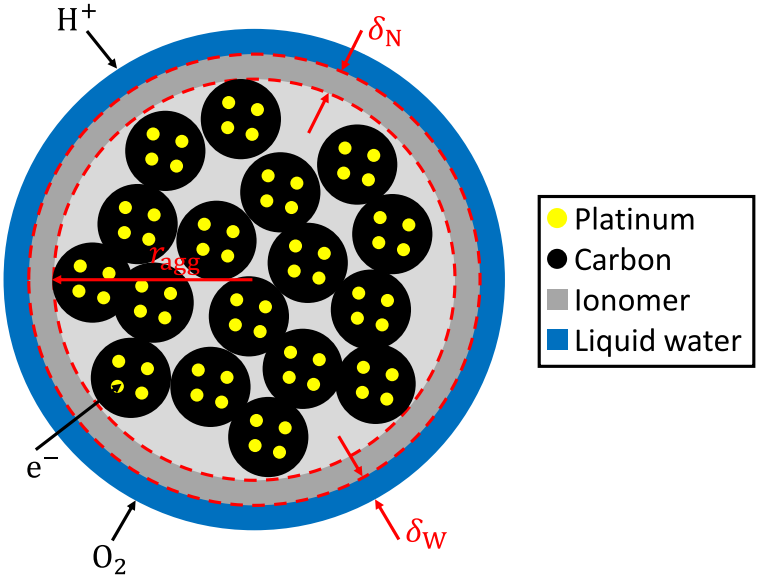

(b) Sketch of an agglomerate

Figure 1. Schematic representation of (a) a single PEMFC cell and (b) a CCL agglomerate.

porous medium, like CL, the effective transport and electrochemical properties depend on its microstructure. For instance, the effective ionic conductivity of CL is related to the volume fraction of ionomer. However, enhanced ionic conductivity (at a constant PtC volume fraction) translates into lower porosity, which lessens the effective reactant diffusivity. Therefore, an appropriate CL composition might provide a balance between the transport and rate processes, which consequently results in an elevated overall cell performance. The described trade-off between different mechanisms gives a rise to an optimization problem.

The aim of this optimization problem is to maximize the membrane electrode assembly (MEA) performance by providing a compromise between the processes occurring in CL. A proper balance between dynamics of these phenomena is obtainable by

Table I. Summary of some selected papers from the literature.

Ref.	Year	Summary of approaches and results
[40]	2000	The impact of catalyst gradients on the performance of the active layer in a PEMFC has been verified through both experimentation and modeling, encompassing both porous and non-porous active layers. The modeling of diffusion and ionic ohmic drop in the cathode's active layer further corroborated the experimental findings, demonstrating that the graded distribution of platinum nanoparticles enhances performance.
[23]	2004	The study employs mathematical modeling and simulation to investigate transport and reaction kinetics in two types of CCL agglomerates: ionomer-filled and water-filled. It reveals that ionomer-filled agglomerates display more consistent reaction rate distributions, while water-flooded agglomerates exhibit high catalyst utilization due to significant proton penetration under specific conditions. The findings highlight the importance of designing an idealized CL composite with hydrophobic secondary pores for effective macroscopic reactant transport and water removal, along with hydrophilized primary micropores for optimal wettability and proton accessibility.
[24]	2006	A model linking spatial distributions, water handling capabilities, and performance is developed using statistical theories and a macro-homogeneous model. The simulation results reveal the sensitivity of CCL operation to various factors, such as porous structure, thickness, wetting angle, and gas pressure. Notably, the findings propose that with favorable parameters (i.e., 10 μm thickness, 5 atm cathode gas pressure, and 89° wetting angle in case of this study), the flooding current density could reach as high as 2 to 3 A cm^{-2}.
[25]	2007	The paper introduces a numerical framework for optimizing cathode electrodes under different operating conditions. By coupling an agglomerate model with a gradient-based optimization algorithm, the study determines the ideal parameters setting. The results highlight that higher platinum loading and moderate electrolyte volume fraction improve performance at low current densities, while reduced platinum loading and increased electrolyte volume fraction and porosity enhance performance at higher current densities. The research also suggests that reducing the solid phase volume fraction in the CL could lead to improved electrode performance.
[41]	2008	The study presents a model for the CCL, incorporating considerations of random porous morphology, transport properties, and electrochemical conversion. Afeedback mechanism triggers a transition from low saturation, which leads to high voltage efficiency, to excessive water accumulation, affecting reaction rate distributions and causing voltage losses. Optimizing the critical current density during this transition enhances both voltage efficiency and power density, with optimal conditions favoring high porosity, a significant fraction of secondary pores, an approximate 90° wetting angle, high gas pressure, and elevated temperature.
[27]	2012	This research explores the oxygen gain in hydrogen fuel cells, which refers to the performance difference observed between cathode fuel streams with varying oxygen levels (depleted and oxygen-rich). The study develops mathematical models to distinguish between mass-transport resistances in CL and GDL medium. Two extreme scenarios are examined: cases where mass transfer limitations occur solely within CL and those external to it, in GDL. In the former situation, oxygen gain values are confined to a finite range, while in the latter, they are unrestricted. The paper proposes a diagnostic technique aimed at identifying the primary source of mass transfer degradation.
[28]	2014	The study develops a model to investigates voltage losses and to explore how agglomerate size and ionomer distribution influence the effectiveness of platinum utilization and the distribution of reaction rates during ORR. The results indicate that smaller agglomerates with higher oxygen pressure at their surface exhibit higher effectiveness factors. Moreover, it is shown that the impact of pore diameter on effectiveness factor is less significant compared to agglomerate size. While the variation of effectiveness factor with ionomer coverage is insignificant within the range of 0.125 to 0.5, higher coverage reduces the effectiveness factor due to increased resistance to oxygen diffusion. Ultimately, the study suggests that a high effectiveness factor is achieved by combining high oxygen pressure, small agglomerate size, and medium ionomer coverage.

controlling the composition of CL. In other words, an appropriate adjustment of volume fractions of constituent materials would improve the performance. As a result, the volume fraction of PtC, volume fraction of ionomer, and porosity could be considered as the decision variables of this optimization problem. Several previous studies in the literature focused on parametric optimization of CL composition. For instance, He et al.[33] investigated the impact of five parameters of the cathode catalyst layer (CCL) on the current-voltage (I-V) relationship of a mathematically modeled PEMFC. These parameters include platinum loading, platinum to carbon (Pt/C) mass ratio, ionomer to carbon (I/C) ratio, carbon particle radius, and electrochemical surface area (ECSA). Their results revealed that platinum loading substantially affects the cell performance. Also, according to their findings, contrary to limiting current density that might be increased by a smaller I/C ratio, a higher value of this parameter is beneficial for enhancing maximum power density. Some other studies[40,42–46] tried to expand parametric analysis by dividing CL into several sub-domains and finding the best composition of CL in a double- or multi-layer configuration. These studies proposed that the cell performance improvement can be achieved with a functionally graded multi-layer design for the catalyst layer.[45] The composition of each sub-layer is controlled independently of other ones with the aim of amplifying the output power. In a more advanced form, Havaej et al.,[35] for instance, compared several non-uniform catalyst loading distribution based on a set of predefined functions. They found that by introducing a non-uniform distribution of catalyst in the longitudinal direction, the cell current density could be increased by 3.1% at a voltage level of 0.2 V. In a recent work, Fan and colleagues[47] used a 1D two-phase model to investigate the impact of graded CL designs on output power and current density distribution of a PEMFC. Despite some improvement in current density uniformity and the output performance, their study is only limited to a linear distribution of ionomer and catalyst within CL. Reviewing the literature clearly shows that a graded or multi-layer design of CL outperforms the simple parametric optimization due to a relatively higher degree of freedom achieved thanks to the heterogeneous distribution of design parameters. However, in graded CL designs, the material distribution function should be usually prescribed in advance. Topology optimization (TO) is a rigorous mathematical optimization technique which provides a high degree of freedom in controlling distribution of decision variables in a given design domain.[48–50] TO can automatically generate spatially graded electrode designs with gradual variations in microstructural topology to achieve favorable MEA performance. In contrast to parametric optimization, which is restricted to adjusting decision variables at a global level while maintaining a uniform distribution, TO allows for control of decision variables values at a local scale.[51–53] Moreover, contrary to the graded designs, TO does not require any material distribution function prior to the optimization. Thus, it is capable of providing various heterogeneous distribution of decision variables while maintaining their global average constant. TO was initially emerged in the field of structural mechanics;[54] however, its application has been then extended to other disciplines, such as fluid-based problems[55] and reaction-diffusion systems.[56,57] To date, the implementation of TO for electrochemical energy devices has been mainly limited to the flow field design[58–60] and thermal

management.[61,62] However, there are only a few number of studies that have investigated the employment of TO for designing innovative electrodes with heterogeneous structures.[63–66] In a recent study, Beck et al.[63] proposed a pioneer non-uniform structure design procedure for electrodes of redox flow batteries based on mathematical optimization. Their findings show that, as compared to conventional electrodes with uniform porosity distribution, using an engineered electrode with varying porosity can increase the efficiency of the battery under various operating conditions. In another study conducted by Deng and Lu,[64] the authors used an optimization algorithm integrated with self-directed online machine learning to obtain the optimal topology of the porous electrode of a lithium-ion battery. By controlling the distribution of solid volume fraction in a 2D electrode, they successfully found a pattern for the structure of the electrode, which leads to 18% increment in the cells maximum specific energy. For the purpose of optimization, they used a 5×5 grid, which is coarser than the mesh used for finite element calculations. Moreover, Lamb and Andrei[65] implemented a gradient-based topology optimization method to achieve the best configuration for the spatial distribution of constituent materials in the catalyst layer of a PEMFC. Unlike,[64] which only considered porosity or solid volume fraction as a decision variable, the researchers in Ref.[65] conducted a multi-variable optimization of catalyst, electrolyte, carbon, and void volume fractions. They reported that in the case of PEMFC, it is desired to increase the volume fraction of catalyst and electrolyte in the region close to the membrane and increase the volume fraction of carbon and voids in the region near the gas diffusion layer (GDL) to obtain higher output voltage. While the study presented in Ref.[65] shows promising results, it is important to note that the use of a single-phase model for simulating the behavior of PEMFC means that the liquid water transport mechanism was not accounted for. Since liquid water has a significant impact on PEMFC characteristics, particularly at high current densities, it is crucial to incorporate a multi-phase model to obtain a more comprehensive understanding and more robust results in the optimization process.

Reviewing the existing research works on optimal design of CL composition shows that there is a relatively small body of literature that is concerned with implementation of powerful mathematical optimization methods, like TO, to find novel electrodes with heterogeneous distribution of constituent materials. The objectives of the present study are to establish a framework for topology optimization of PEMFC electrode and to explore the optimal CL structure that provides an appropriate balance between dynamics of transport and rate processes, which as a result might enhance the overall cell performance. To accomplish this goal, first, a 2D two-phase model of PEMFC is developed that captures major electrochemical and transport phenomena of PEMFC. By considering the liquid water transfer in PEMFC, the proposed model is capable of accurately simulating the cell behavior even at high current densities. The model is then validated against experimental data to ensure the precision of the proposed mathematical formulation. Next, a topology optimization algorithm based on density model[67] is used to obtain the best structure of CCL in a given design domain with the aim of increasing the output current density at a constant cell voltage. Whilst the models that were used in the previous TO studies, such as,[65] dominantly suffered from a lack of two-phase flow effects, this gap is filled by adoption of a robust mathematical description of PEMFC performance that considers those mechanisms. Hence, the findings of this research are more reliable and consistent than those reported in the literature. However, it is noteworthy that the primary aim of this study is establishment of an optimization procedure that seeks optimized structure for CL of PEMFC rather than overstated claims. The readers should bear in mind that some limitations are present in the current cell-scale modeling of PEMFC in the literature. For instance, the electrode properties (e.g. porosity) vary between the regions beneath the rib and beneath the channel due to differences in compression during the cell assembly process. However, most modeling studies in the literature assume uniform properties across these regions. Those details are beyond the scope of this study, as the current work primarily focuses on applying TO to achieve optimized material distribution in the CL. Finally, PEMFC performance improvement as a result of the optimized CL structure will be discussed in terms of electrochemical aspects and transport phenomena.

The following parts of this paper is divided into five sections. Section Mathematical Modeling deals with modeling of PEMFC, where the governing equations used in the present work are described. In addition, a brief explanation of various categories of PEMFC modeling that exists in the literature is provided. All the processes considered in this model are descried and their relevant mathematical correlations are provided. Section Topology Optimization reviews the topology optimization procedure and presents the optimization problem formulation with an explanation of the objective function and constraints. In Section Results and Discussion, first, the developed model is validated against experimental results. Afterwards, the results obtained from the optimization process are given together with a comprehensive discussion of electrochemical and transport phenomena. Finally, the conclusion of this paper is drawn in Section Conclusions.

Mathematical Modeling

In the present study, a two-phase flow, non-isothermal model is developed to simulate the performance of the PEMFC. The computational domain is shown in Fig. 1a. The model considers the flow channel as well as five layers of the cell, including two GDLs, two CLs, and a proton exchange membrane (PEM). The governing equations are given as follows.

Conservation of mass and species:

The conservation of species and mass for gaseous are described by the Maxwell-Stefan and Brinkman equations, respectively.[68,69] The Maxwell-Stefan, mass continuity, and Brinkman equations are given as:

$$\rho\mathbf{u}\cdot\nabla\omega_{\mathrm{i}} - \nabla\cdot\left(\rho\omega_{\mathrm{i}}\sum_{\mathrm{k}} D_{\mathrm{ik}}\left[\nabla x_{\mathrm{k}} + (x_{\mathrm{k}} - \omega_{\mathrm{i}})\frac{\nabla p}{p}\right] + D_{\mathrm{i}}^{\mathrm{T}}\frac{\nabla T}{T}\right) = M_{\mathrm{i}}R_{\mathrm{i}} \quad [1]$$

$$\nabla\cdot(\rho\mathbf{u}) = Q_{\mathrm{m}} \quad [2]$$

$$\frac{\rho}{\varepsilon_{\mathrm{void}}}\left(\mathbf{u}\cdot\nabla\frac{\mathbf{u}}{\varepsilon_{\mathrm{void}}}\right) = -\nabla p + \nabla\cdot\left[\frac{\mu}{\varepsilon_{\mathrm{void}}}\left\{(\nabla\mathbf{u} + (\nabla\mathbf{u})^{\mathrm{T}}) - \frac{2}{3}(\nabla\cdot\mathbf{u})\mathbf{I}\right\}\right] - \left(\mu\kappa^{-1} + \frac{Q_{\mathrm{m}}}{\varepsilon_{\mathrm{void}}^2}\right)\mathbf{u} \quad [3]$$

in which $\mathbf{u}$ is velocity (m s^{-1}), p is pressure (Pa), T is temperature (K), ρ is density (kg m^{-3}), and μ is viscosity (Pa s) of the gaseous mixture. In addition, ω, x, D^{T}, M, ε_{v}, and κ are mass fraction, mole fraction, thermal diffusion coefficient (kg m^{-1} s^{-1}), molecular weight (kg mol^{-1}), porosity, and permeability (m^2), respectively. D_{ik} is multi-component diffusivity (m^2 s^{-1}). The subscripts i and k denotes the gas species. Also, R and Q_{m} represent the source terms.

Liquid water transport:

The liquid water transport equation is expressed by:

$$-\nabla\cdot(D_{\mathrm{cap}}\nabla C_{\mathrm{lw}}) + \mathbf{u}\nabla C_{\mathrm{lw}} = R_{\mathrm{lw}} \quad [4]$$

where C_{lw} is liquid water concentration (mol m^{-3}) and D_{cap} is capillary diffusivity (m^2 s^{-1}). The source term, R_{lw}, is determined by the rate of water condensation and evaporation in the cell.

However, in CCL, where ORR is taking place, the produced liquid water is also contributing to this source term. The water saturation, s_{lw}, is correlated to the liquid water concentration through the following relationship.

$$s_{lw} = \frac{M_{H_2O}}{\varepsilon_{void}\rho_{lw}} C_{lw} \quad [5]$$

Dissolved water transport:

The transport of dissolved water through membrane/ionomer in ACL, PEM, and CCL is given by:

$$-\nabla\cdot(D_{dw}C_{dw}) = S_d \quad [6]$$

In Eq. 6, D_{dw} and C_{dw} are dissolved water diffusivity ($m^2\ s^{-1}$) and dissolved water concentration (mol m^{-3}), respectively. The boundary conditions required for solving this equation are calculated based on the relative humidity level (RH) at the interface between CL and GDL. The dissolved water concentration at this interface is formulated as:[69]

$$C_{dw}|_{CL/GDL} = (0.043 + 17.81RH - 39.85RH^2 + 36.0RH^3)\frac{\rho_m}{EW} \quad [7]$$

where ρ_m is density of ionomer/membrane (kg m^{-3}) and EW is the equivalent weight of ionomer/membrane (kg mol^{-1}).

Conservation of energy:

Given the assumption that all phases are in thermal equilibrium, the energy conservation is governed by:[62,68]

$$\nabla\cdot\left(\sum_{i=g,l}[\rho c_p \mathbf{u}]_i T\right) - \nabla\cdot\left(\sum_{i=g,l,s} k_i \nabla T\right) = S_T \quad [8]$$

where c_p and k are specific heat capacity (J $mol^{-1}\ K^{-1}$) and thermal conductivity (W $m^{-1}\ K^{-1}$), respectively. The subscript i denotes the gas mixture, liquid water, and solid phase. It is noteworthy that the energy source term, S_T, is a summation of heat generation/consumption by electrochemical reaction, Joule heating, and the water phase change process. All source terms are listed in Table II.

Conservation of charge:

The electrons and protons are transferred through carbon-supported platinum and ionomer, respectively. The electron transport in GDLs and CLs of both anode and cathode sides, as well as proton transport in CLs and PEM, is modeled by Ohms law. The conservation of charges are expressed by:

$$\nabla\cdot(-\sigma_s^{eff}\nabla\phi_s) = -i_{src.} \quad [9]$$

$$\nabla\cdot(-\sigma_m^{eff}\nabla\phi_m) = i_{src} \quad [10]$$

in which σ_s^{eff} and σ_m^{eff} are effective electric and ionic conductivities (S m^{-1}), respectively. Moreover, ϕ_s and ϕ_m are solid and electrolyte phases potentials (V), respectively, and i_{src} is volumetric current density source (A m^{-3}). The current density source is zero within both the GDLs and PEM. The calculation of i_{src} within the CLs is addressed in the next subsection.

Agglomerate model.—A spherical agglomerate sub-model (see Fig. 1b), adopted from,[68–71] is utilized to determine the electrochemical kinetics. It is assumed that the agglomerate is covered with a thin ionomer film. Moreover, owing to the hydrophilic properties of the ionomer, the liquid water produced during the electrochemical reaction is considered to form an additional layer, overlaying the ionomer film.[69] The ionomer film thickness is treated as an input for the model, whereas the water film thickness is calculated based on the liquid water saturation, as described in a subsequent equation. Previous experimental and numerical studies reported various values for the thickness of ionomer film, spanning from a few nanometers to as much as 100 nm.[72–75] Moreover, although microscopy studies[76,77] reported a value between 50 to 170 nm for the agglomerate radius, numerical studies typically reported larger values in a range between 50 and 5000 nm.[68,73,75,78] This occurs because, in cell-scale modeling, the intricate microstructure of CL is substituted with volume-averaged characteristics, like porosity. Consequently, certain adjustments or fittings are necessary to mimic the experimental performance results. The summation of constituent volume fractions in CL is as follows:

$$\varepsilon_{PtC} + \varepsilon_1 + \varepsilon_{void} = 1 \quad [11]$$

where ε_{PtC} and ε_1 are volume fractions of carbon-supported platinum and ionomer, respectively. The volume fraction of platinum and carbon might be separated according to Eqs. 12 and 13.

Table II. Source terms.

Source terms	Domain
$Q_m = M_{H_2}S_{H_2} + M_{O_2}S_{O_2} + M_{H_2O}S^v_{H_2O}$	GDLs and CLs
$S_{H_2} = \frac{i^a_{src}}{2F}$	ACL
$S_{O_2} = \frac{i^c_{src}}{4F}$	CCL
$S^v_{H_2O} = \begin{cases} h_{cond}\frac{\varepsilon_{void}(1-s_{lw})x^v_{H_2O}}{RT}(x^v_{H_2O}p - p^{sat}) & \text{if } x^v_{H_2O}p \geqslant p^{sat} \\ h_{evp}C_{lw}(p^{sat} - x^v_{H_2O}p) & \text{if } x^v_{H_2O}p < p^{sat} \end{cases}$	GDLs and CLs
$R^{rxn}_{lw} = \frac{i^a_{src}}{2F}$	CCL
$S_d = h_{mass}(C_{H_2O} - C_{wp})$	CLs
$S^{electric}_{T,\ joule} = \frac{i^2_{electric}}{\sigma_s^{eff}}$	GDLs and CLs
$S^{ionic}_{T,\ joule} = \frac{i^2_{ionic}}{\sigma_m^{eff}}$	CLs and PEM
$S^a_{T,\ rxn} = \lvert i^a_{src}\rvert(\lvert\eta^a\rvert - \frac{T\Delta S^a}{2F})$	ACL
$S^c_{T,\ rxn} = \lvert i^c_{src}\rvert(\lvert\eta^c\rvert - \frac{T\Delta S^c}{4F})$	CCL
$S_{T,\ phase} = M_{H_2O}S^v_{H_2O}\Delta h_{H_2O}$	GDLs and CLs

$$\varepsilon_{Pt} = \frac{m_{Pt}}{t_{CL}\rho_{Pt}} \quad [12]$$

$$\varepsilon_{C} = \frac{m_{Pt}(1-\gamma_{PtC})}{\gamma_{PtC} t_{CL}\rho_{C}} \quad [13]$$

in which m_{Pt} is platinum loading (kg m^{-2}), t_{CL} is thickness of CL (m), ρ_{Pt} and ρ_{C} are platinum and carbon densities (kg m^{-3}), and γ_{PtC} is platinum mass fraction. Knowing the carbon loading m_{C} (kg m^{-2}), the platinum mass fraction is expressed as:

$$\gamma_{PtC} = \frac{m_{Pt}}{m_{Pt} + m_{C}} \quad [14]$$

The radius of agglomerate r_{agg} and thickness of ionomer film δ_{N} (m) are given as model input. The agglomerate density, which is defined as the number of agglomerates per unit volume of CL, reads as:

$$N_{agg} = \frac{1-\varepsilon_{void}}{\frac{4}{3}\pi(r_{agg}+\delta_{N})^{3}} \quad [15]$$

The specific surface area of agglomerate with water coating is given by:

$$a'_{agg} = a_{agg}\left(\frac{r_{agg}+\delta_{N}+\delta_{W}}{r_{agg}+\delta_{N}}\right)^{2} \quad [16]$$

where a_{agg} and a'_{agg} are specific surface area of agglomerate without and with water coating (m^{-1}), respectively, and δ_{W} is the thickness of liquid water coating (m) covering the agglomerate. The value of a_{agg} is computed by:

$$a_{agg} = 4\pi N_{agg}(r_{agg}+\delta_{N})^{2} \quad [17]$$

Knowing that Nafion ionomer is hydrophilic, it is assumed that the generated water by the electrochemical reaction forms a liquid water coating on the ionomer film.[69] The thickness of liquid water coating is estimated by:[69]

$$\delta_{W} = \sqrt[3]{(r_{agg}+\delta_{N})^{3} + \frac{s_{lw}\varepsilon_{void}}{\frac{4}{3}\pi N_{agg}}} - (r_{agg}+\delta_{N}) \quad [18]$$

For CCL, the volumetric current density source is expressed by:[69,70]

$$i^{c}_{src} = 4F\frac{P_{O_2}}{H_{O_2}}\left[\frac{1}{E_{r}k_{c}\frac{r^{3}_{agg}a_{agg}}{(r_{agg}+\delta_{N})^{2}}} + \frac{(r_{agg}+\delta)}{\xi r_{agg}}\right]^{-1} \quad [19]$$

in which

$$\delta = \delta_{N} + \delta_{W} \quad [20]$$

and

$$\xi = \frac{\xi_{N}\xi_{W}}{\xi_{N}+\xi_{W}} \quad [21]$$

$$\xi_{N} = \frac{a_{agg}D_{O_2-N}}{\delta_{N}} \quad [22]$$

$$\xi_{W} = \frac{a'_{agg}D_{O_2-W}}{\delta_{W}} \quad [23]$$

where D_{O_2-N} and D_{O_2-W} are diffusivity of oxygen in ionomer and water (m^{2} s^{-1}), respectively. In Eq. 19, P_{O_2} is oxygen partial pressure (Pa) and H_{O_2} is Henry's constant for oxygen dissolution (Pa m^{3} mol^{-1}). In addition, the reaction rate coefficient (k_{c}) and effectiveness factor (E_{r}) in this equation are calculated as follows:[69]

$$k_{c} = \frac{A_{Pt}}{4F(1-\varepsilon_{void})}\left(\frac{i_{0,c}}{C^{ref}_{O_2}}\right)\left[-\exp\left(\frac{(1-\alpha_{c})F\eta_{c}}{RT}\right) + \exp\left(\frac{-\alpha_{c}F\eta_{c}}{RT}\right)\right] \quad [24]$$

$$E_{r} = \frac{1}{Th}\left[\frac{1}{\tanh(Th)} - \frac{1}{Th}\right] \quad [25]$$

in which A_{Pt} is total reaction area per unit volume of agglomerate (m^{-1}), $i_{0,c}$ is exchange current density for oxygen reduction reaction (A m^{-2}), $C^{ref}_{O_2}$ is oxygen reference concentration (mol m^{-3}), α_{c} is cathode charge transfer coefficient, η_{c} is cathode overpotential (V), R is gas constant (J mol^{-1} K^{-1}), and Th is Thiele modulus. It is noteworthy that the dependence of ORR rate on the local concentration (pressure) of oxygen is considered in Eq. 19. The temperature dependence of exchange current density is expressed using an Arrhenius relationship as:[79]

$$i_{0,c} = i^{ref}_{0,c}\exp\left[-\frac{E_{a}}{RT}\left(1-\frac{T}{T^{ref}}\right)\right] \quad [26]$$

where $i^{ref}_{0,c}$, E_{a}, and T^{ref} are reference exchange current density (A m^{-2}), activation energy (J mol^{-1}), and reference temperature (K). The activation energy of ORR on platinum is 66000 J mol^{-1}.[79] In addition, A_{Pt} reads as:[69]

$$A_{Pt} = A_{0}\frac{m_{Pt}}{t_{CL}} \quad [27]$$

where A_{0} (m^{2} kg^{-1}) is given by the following empirical relationship as a function of platinum mass fraction.[69,70]

$$A_{0} = [2.2779\gamma^{3}_{PtC} - 1.5857\gamma^{2}_{PtC} - 2.0153\gamma_{PtC} + 1.5950] \times 10^{5} \quad [28]$$

Additionally, Thiele modulus is evaluated as:

$$Th = r_{agg}\sqrt{\frac{k_{c}}{D^{eff}_{agg}}} \quad [29]$$

where D^{eff}_{agg} is effective diffusivity of oxygen within agglomerate (m^{2} s^{-1}) and is computed based on Bruggeman equation as follows:

$$D^{eff}_{agg} = D_{O_2-N} \times \varepsilon^{1.5}_{agg} \quad [30]$$

In Eq. 30, ε_{agg} is fraction of agglomerate volume filled with ionomer and might be evaluated as:

$$\varepsilon_{agg} = 1 - \left(\frac{\varepsilon_{PtC}}{\frac{4}{3}\pi N_{agg} r^{3}_{agg}}\right) \quad [31]$$

For ACL, the hydrogen reduction kinetics follows the well-known Butler-Volmer relationship as:[69]

$$i_{\mathrm{src}}^{\mathrm{a}} = A_{\mathrm{Pt}} i_{0,\mathrm{a}}^{\mathrm{ref}} \left(\frac{1-\varepsilon_{\mathrm{void}}}{\varepsilon_{\mathrm{PtC}}}\right)\left(\frac{P_{\mathrm{H_2}}}{H_{\mathrm{H_2}} C_{\mathrm{H_2}}^{\mathrm{ref}}}\right)^{0.5}\left[\exp\left(\frac{\alpha_{\mathrm{a}} F \eta_{\mathrm{a}}}{RT}\right) - \exp\left(\frac{-(1-\alpha_{\mathrm{a}}) F \eta_{\mathrm{a}}}{RT}\right)\right] \quad [32]$$

in which $i_{0,\mathrm{a}}^{\mathrm{ref}}$ is anode exchange current density, $P_{\mathrm{H_2}}$ is hydrogen partial pressure (Pa), $H_{\mathrm{H_2}}$ is Henry's constant for hydrogen dissolution (Pa $\mathrm{m^3\ mol^{-1}}$), and $C_{\mathrm{H_2}}^{\mathrm{ref}}$ is hydrogen reference concentration (mol $\mathrm{m^{-3}}$). Moreover, α_{a} is anode charge transfer coefficient and η_{a} is anode overpotential (V). Since anode charge transfer coefficient and anode exchange current density exhibit weak dependence on temperature, they are considered constant across various operating temperatures.[69] However, considering the relatively greater influence of temperature on the cathode charge transfer coefficient, this parameter was fine-tuned during the validation process to achieve results that effectively replicate the experimental data.[69] For both anode and cathode CLs, activation overpotential is given by:

$$\eta = \phi_{\mathrm{s}} - \phi_{\mathrm{m}} - E^{\mathrm{eq}} \quad [33]$$

where E^{eq} is equilibrium potential (V). A list of additional relationships and physical properties are given in Tables III and IV.

Boundary conditions.—The electric potential on the anode rib (A − A′ and A″ − A‴) and cathode rib (F − F′ and F″ − F‴) are defined as Dirichlet boundary conditions. The value on anode side is set to be zero and on the cathode side corresponds to the cell voltage. The dissolved water concentration at the CL/GDL interface for both anode and cathode sides (B − B′ and D − D′) are defined as Dirichlet boundary condition according to Eq. 7. The conditions at anode inlet (A′ − A″) and anode rib (A − A′ and A″ − A‴) are given by:

$$p = p_{\mathrm{a}};\ x_{\mathrm{H_2O},a}^{0} = \frac{P^{\mathrm{sat}}\mathrm{RH_a}}{p_{\mathrm{a}}};\ x_{\mathrm{H_2},a}^{0} = 1 - x_{\mathrm{H_2O},a}^{0};\ T = T_{\mathrm{a}}^{0} \quad [34]$$

in which x represents the mole fraction. Likewise, the boundary condition at cathode inlet (F′ − F″) and cathode rib (F − F′ and F″ − F‴) are expressed as:

$$p = p_{\mathrm{c}};\ x_{\mathrm{H_2O},c}^{0} = \frac{P^{\mathrm{sat}}\mathrm{RH_c}}{p_{\mathrm{c}}};\ x_{\mathrm{O_2},c}^{0} = 0.21(1 - x_{\mathrm{H_2O},c}^{0});\ x_{\mathrm{N_2},c}^{0} = 0.79(1 - x_{\mathrm{H_2O},c}^{0});\ T = T_{\mathrm{c}}^{0} \quad [35]$$

The liquid water saturation at the cathode inlet (F′ − F″) is set to be zero. A symmetry boundary condition is considered for all other boundaries.

Topology Optimization

TO is a relatively more advanced method compared to other conventional optimization techniques, such as shape and size optimizations. Compared to other optimization approaches that usually focus on globally tuning a set of decision variables to maximize or minimize one or more objective functions, TO stands out for its ability to finely control those variables at a local level. From this standpoint, the higher degree of freedom provided by TO makes it a robust and strong optimization tool. TO considers optimization process as a material distribution problem and seeks to generate creative layouts within a defined design domain to either maximize or minimize a specified objective function. In this sense, a material allocation problem might mathematically read as:

$$\theta(\mathbf{x}) = \begin{cases} 1 & \text{if } \mathbf{x} \in \Omega_{\mathrm{M}} \\ 0 & \text{if } \mathbf{x} \in \Omega \backslash \Omega_{\mathrm{M}} \end{cases} \quad [36]$$

in which $\mathbf{x}$ is any position in the given design domain (Ω) and θ is a material distribution function. The distribution θ takes a value of one ($\theta = 1$) in regions where material exists (Ω_{M}), while it is set to zero

Table III. Additional relationships and definitions.

Description	Equation	Unit
Ionic conductivity[68]	$\sigma_{\mathrm{m}}^{0} = (0.514\lambda - 0.326)\exp\left[1268\left(\frac{1}{303} - \frac{1}{T}\right)\right]$	S $\mathrm{m^{-1}}$
Effective ionic conductivity[68]	$\sigma_{\mathrm{m}}^{\mathrm{eff}} = \sigma_{\mathrm{m}}^{0}\varepsilon_{\mathrm{l}}^{1.5}$	S $\mathrm{m^{-1}}$
Effective electric conductivity[68]	$\sigma_{\mathrm{s}}^{\mathrm{eff}} = \sigma_{\mathrm{s}}^{0}\varepsilon_{\mathrm{PtC}}^{1.5}$, $\sigma_{\mathrm{s}}^{\mathrm{eff}} = \sigma_{\mathrm{s}}^{0}(1 - \varepsilon_{\mathrm{void}}^{\mathrm{GDL}})^{1.5}$	S $\mathrm{m^{-1}}$
Water content[80]	$\lambda = \frac{EW}{\rho_{\mathrm{m}}} C_{\mathrm{dw}}$	–
Dissolved water diffusivity[68]	$D_{\mathrm{dw}} = 10^{-10}\exp\left[2416\left(\frac{1}{303} - \frac{1}{T}\right)\right]\begin{cases} 2.05\lambda - 3.25 & \text{for } 2 \leqslant \lambda < 3 \\ 6.65 - 1.25\lambda & \text{for } 3 \leqslant \lambda < 4 \\ 2.563 - 0.33\lambda + 0.0264\lambda^2 - 0.000671\lambda^3 & \text{for } \lambda \geqslant 4 \end{cases}$	$\mathrm{m^2\ s^{-1}}$
Effective porosity	$\varepsilon_{\mathrm{void}}^{\mathrm{eff}} = \varepsilon_{\mathrm{void}}(1 - s_{\mathrm{lw}})$	–
Leverett function[69]	$J = \begin{cases} 1.417(1 - s_{\mathrm{lw}}) - 2.120(1 - s_{\mathrm{lw}})^2 + 1.263(1 - s_{\mathrm{lw}})^3 & \text{for } \theta < 90^\circ \\ 1.417 s_{\mathrm{lw}} - 2.120 s_{\mathrm{lw}}^2 + 1.263 s_{\mathrm{lw}}^3 & \text{for } \theta > 90^\circ \end{cases}$	–
Capillary pressure[68]	$P_{\mathrm{cap}} = \sigma_{\mathrm{lw}}\cos(\theta)\left(\frac{\varepsilon_{\mathrm{void}}}{\kappa}\right)^{0.5} J$	Pa
Saturation pressure[69]	$P^{\mathrm{sat}} = 10^{[-2.1794 + 0.029\,53(T - 273.15) - 9.1837\times10^{-5}(T-273.15)^2 + 1.4454\times10^{-7}(T-273.15)^3]}$	Pa
Relative permeability[68]	$\kappa_{\mathrm{l}}^{\mathrm{rel}} = \kappa s_{\mathrm{lw}}^{3}$	$\mathrm{m^2}$
Capillary diffusivity[68]	$D_{\mathrm{cap}} = -\frac{\kappa_{\mathrm{l}}^{\mathrm{rel}}}{\mu_{\mathrm{lw}}}\left(\frac{\partial P_{\mathrm{cap}}}{\partial s_{\mathrm{lw}}}\right)$	$\mathrm{m^2\ s^{-1}}$
Cathode equilibrium potential[69]	$E_{\mathrm{c}}^{\mathrm{eq}} = 1.482 - 8.45\times10^{-4}T + 4.31\times10^{-5}T\ln(p_{\mathrm{H_2}}p_{\mathrm{O_2}}^{0.5})$	V
Equilibrium vapor concentration[81]	$C_{\mathrm{wp}} = \frac{P^{\mathrm{sat}}}{RT}a$	mol $\mathrm{m^{-3}}$

Table IV. Physical and transport properties.

Parameter	Symbol	Value/Expression	Unit
Platinum density[69]	ρ_{Pt}	21 450	kg m^{-3}
Carbon density[69]	ρ_{C}	2000	kg m^{-3}
Ionomer density[69]	ρ_{m}	1800	kg m^{-3}
Ionomer equivalent weight[69]	EW	1.1	kg mol^{-1}
Permeability (GDL, CL)[69]	κ	4.97×10^{-13}, $4.97 \times 10^{-13}(\varepsilon_{void}^{CL}/\varepsilon_{void}^{GDL})^{1.5}$	m^2
Agglomerate radius[75]	r_{agg}	7×10^{-7}	m
Ionomer film thickness[72]	δ_N	7×10^{-9}	m
Oxygen reference concentration[82]	$C_{O_2}^{ref}$	3.39	mol m^{-3}
Hydrogen reference concentration[82]	$C_{H_2}^{ref}$	56.4	mol m^{-3}
Water surface tension coefficient[82]	σ_{lw}	0.0625	N m^{-1}
Evaporation rate constant[69]	h_{evp}	100	atm^{-1} s^{-1}
Condensation rate constant[69]	h_{cond}	100	s^{-1}
Electric conductivity[69]	σ_s^0	1250	S m^{-1}
Latent heat of condensation/evaporation[69]	Δh_{H_2O}	2.308×10^6	J kg^{-1}
Entropy of hydrogen oxidation[69]	ΔS^a	161.2	J mol^{-1} K^{-1}
Entropy of oxygen reduction[69]	ΔS^a	−324	J mol^{-1} K^{-1}

($\theta = 0$) in void regions. Given the fact that working with a discontinuous function is mathematically troublesome, a "density method"[67] is usually used in real applications. This method replaces the discontinuous function, θ, with an analogous continuous density function, θ_C, which can take any value between zero and one ($0 \leqslant \theta_C(\mathbf{x}) \leqslant 1$). In structural mechanics problem, where any intermediate value for the density function (other than zero or one) is physically meaningless, some additional considerations, such as "Simplified Isotropic Material with Penalization" (SIMP) method,[67] are taken into account to obtain a more accurate correlation between density value and material properties. However, in this study, as we are working with volume fraction of constituent materials (rather than Boolean-type distribution of materials), the effective material properties are correlated to the volume fraction of corresponding materials through power-law relationships as expressed in Table III. In other words, a power-law (Bruggeman equation) penalization scheme is utilized to reflect the effect of TO homogenization on the material parameters in the governing equations. Standard regularization methods are implemented on optimization solutions to prevent the checkerboard pattern problem. It is a well-studied problem in the field of TO[83–85] and has been resolved by utilization of solution filtering and projection. This research exploits a Helmholtz-type filter[83] as well as a hyperbolic tangent projection[86] to address this problem. Helmholtz filter is expressed as a solution to the following partial differential equation (PDE).

$$\begin{aligned} -R_f^2 \nabla^2 \tilde{\theta}_C(\mathbf{x}) + \tilde{\theta}_C(\mathbf{x}) &= \theta_C(\mathbf{x}) \\ \nabla \tilde{\theta}_C \cdot \hat{\mathbf{n}} &= 0 \quad \text{on } \Gamma \end{aligned} \tag{37}$$

In Eq. 37, $\tilde{\theta}_C$ and R_f are filtered density function and the filter radius, respectively. To obtain filtered density function, Helmholtz PDE should be solved based on a homogeneous Neumann boundary condition, as shown in the above equation (Γ is the boundary of the design domain). Additionally, a hyperbolic tangent projection[86] is used to further regulate the optimization solutions, as follows:

$$\tilde{\tilde{\theta}}_C = \frac{\tanh(\beta(\tilde{\theta}_C - \theta_\beta)) + \tanh(\beta\theta_\beta)}{\tanh(\beta(1 - \theta_\beta)) + \tanh(\beta\theta_\beta)} \tag{38}$$

where $\tilde{\tilde{\theta}}_C$ is the density function after projection, and β and θ_β are projection tuning parameters. In the literature, β is called projection steepness and θ_β is known as projection point. Next, "globally convergent method of moving asymptotes" (GCMMA) algorithm[87] is used to update the decision variables. GCMMA is a gradient-based algorithm; as a consequence, the sensitivity of objective function with respect to the decision variables should be calculated. Sensitivity analysis is performed using the adjoint state method.[88] Contrary to other approaches, like forward method, which are computationally expensive, the adjoint method is independent of the number of the decision variables. Hence, it is a very efficient technique from the computational perspective, which makes it especially suitable for TO problems that typically include numerous decision variables. According to this method, the total derivative of an objective function (F_{obj}) with respect to each decision variable, ζ_i, is indicated as:

$$\frac{dF_{obj}}{d\zeta_i} = \frac{\partial F_{obj}}{\partial \zeta_i} + \boldsymbol{\lambda}^T \frac{\partial \mathbf{G}}{\partial \zeta_i} \tag{39}$$

in which $\boldsymbol{\lambda}$ is the vector of adjoint variables and $\mathbf{G}$ is the system of governing PDEs. As this study deals with CL structure optimization, the decision variables (ζ) are considered being volume fractions of PtC (ε_{PtC}) and ionomer (ε_I). The adjoint variables are given as the solution to the following adjoint equation:

$$\left(\frac{\partial \mathbf{G}}{\partial \mathbf{U}}\right)^T \boldsymbol{\lambda} = -\left(\frac{\partial F_{obj}}{\partial \mathbf{U}}\right)^T \tag{40}$$

where $\mathbf{U}$ is a vector of state variables that are determined from the governing equations.

Problem formulation.—As previously mentioned, the performance of PEMFC depends on several coupled transport and rate processes that are taking place in the cell. In such a situation, the overall cell performance is dictated by the slowest process. For instance, the rate of an electrochemical reaction not only depends on charge transfer rate but also is affected by the rate at which reactant species are supplied (or product species are removed). The effective transport and rate properties of CL might be controlled by the volume fraction of constituent materials. For example, a very high volume fraction of PtC is beneficial to increase the rate of reactant consumption. On the other hand, this means a lower porosity, which in return causes sluggish gas transport. A huge drop in reactant delivery might deteriorate the overall cell performance. Hence, the composition of CL should be adjusted in a way that a compromise would be obtained between various processes. The output power density of PEMFC, which indicates the cell performance, could be estimated knowing the cell voltage and current density. At any specific current density, the cell voltage can be calculated using the governing equations expressed in Section Mathematical Modeling.

Therefore, at any given current density, a superior performance might be achieved if the overpotential is decreased and consequently, the cell voltage is increased. The optimization problem at a given current density ($I_{\text{cell}}^{\text{in}}$) is defined as:

$$\begin{aligned} \max_{\varepsilon_{\text{PtC}},\varepsilon_{\text{l}}} \quad & F_{\text{obj}} = V_{\text{cell}}|_{@\ I_{\text{cell}}^{\text{in}}} \\ \text{s.t.} \quad & \varepsilon_{\text{PtC}}(\mathbf{x}) + \varepsilon_{\text{l}}(\mathbf{x}) + \varepsilon_{\text{void}}(\mathbf{x}) = 1 \quad \forall \mathbf{x} \in \Omega_{\text{CCL}} \\ & 0 \leqslant \varepsilon_{\text{PtC}}(\mathbf{x}) \text{ and } \varepsilon_{\text{l}}(\mathbf{x}) \leqslant 1 \quad \forall \mathbf{x} \in \Omega_{\text{CCL}} \\ & 0 \leqslant m_{\text{Pt}}^{\text{avg}} \leqslant m_{\text{Pt}}^{\text{max}} \\ & 0 \leqslant \varepsilon_{\text{l}}^{\text{avg}} \leqslant \varepsilon_{\text{l}}^{\text{max}} \end{aligned} \quad [41]$$

where Ω_{CCL} is the CCL domain. Since the overpotential in CCL is greater than that of the anode catalyst layer (ACL), this study only focuses on the spatial structure of this component. However, the described procedure might be applied to any other component of PEMFC by considering appropriate decision variables. Furthermore, according to the formulation of Eq. 41, the optimization objective is defined as maximization of the cell voltage at a specific current density $I_{\text{cell}}^{\text{in}}$. The optimization problem is subject to some physical and design constraint as shown in Eq. 41. First, at the local level, a physical constraint applies to any position $\mathbf{x}$ in the CCL domain, which requires that the summation of volume fractions of constituents adds up to one. Additionally, by definition, the volume fraction of each decision variable cannot be more than unity at a local level. In practical implementation, the optimization algorithm updates the value of decision variables (ε_{PtC} and ε_{l}) in each iteration while calculating the porosity automatically through $\varepsilon_{\text{void}} = 1 - (\varepsilon_{\text{PtC}} + \varepsilon_{\text{l}})$. At a global level, the optimization problem might be subject to some additional constraints. In the present study, the problem is formulated so that the average mass loading of platinum ($m_{\text{Pt}}^{\text{avg}}$) and average ionomer volume fraction ($\varepsilon_{\text{l}}^{\text{avg}}$) over the entire CCL do not exceed a maximum value ($m_{\text{Pt}}^{\text{max}}$ and $\varepsilon_{\text{l}}^{\text{max}}$). A major difference between parametric and TO rises from the fact that parametric optimization can only control the average mass loading (or average volume fraction) of constituent materials; however, TO not only controls the average mass loading but also adjusts their distribution. When performing parametric optimization, a higher loading of platinum or ionomer may lead to enhanced output power. Nevertheless, it should be noted that a higher platinum (or ionomer) loading implies more expensive cell as well. Opposed to conventional parametric optimization, TO does not necessarily improve CL design by using more amount of platinum or ionomer. However, it promotes the cell performance through more effective distribution of the available materials. It is also noteworthy that while the previously introduced density function (θ_{C}) does not appear explicitly in the optimization problem Eq. 41, a unique density function is assigned for determination of each decision variable during the optimization process. In this regard, the decision variables (ε_{PtC} and ε_{l}) are updated according to the value of their relevant density function after regularization.

Numerical implementation.—The numerical procedure used in the present study to find the optimal CL design is as follows. The mathematical model developed in the previous Section is implemented in COMSOL Multiphysics® (version 5.6) software to solve the governing equations by a finite element method. The parameters used in this study are tabulated in Table V. By solving these equations for a wide range of current densities, polarization characteristics of the PEMFC are obtained. The obtained I-V is then compared to an experimental data set to confirm the validity of the proposed model. Next, an optimization is conducted to obtain the optimal distribution of material in CCL. TO process begins with initialization of the design variables and evaluation of the objective function according to Eq. 41. Next, the sensitivity (gradient) of objective function with respect to the design variables is computed. By regularization of the design variables using a Helmholtz filtering and hyperbolic tangent projection schemes, the optimization process is continued. In the subsequent step, the GCMMA algorithm is used to update the design variables. As the measured sensitivity has a different value at each position in the calculation domain, the design variables are updated at a local level accordingly. Hence, the updated values of design variables vary with the position, which gives a rise to a heterogeneous layout. TO favors non-uniform distribution of design variables in order to maximize the objective function. In other words, it enhances utilization of the constituent materials by placing them in areas that they are needed more. This iterative procedure is repeated till the maximum number of iterations is reached. In summary, the optimization process is described as follows:

Step 1:The PEMFC model, related parameters, and the design variables are initialized.
Step 2:The mathematical model is solved at a given current density and the objective function is computed according to Eq. 41.
Step 3:A sensitivity analysis is performed using the adjoint variable method to calculate the gradient of objective function with respect to the design variables.
Step 4:A regularization process is conduced to smooth the design solutions over the calculation domain.
Step 5:Using the GCMMA method, the design variables are updated.
Step 6:If the maximum number of iterations is reached, the optimization process is terminated. Otherwise, steps 2 to 5 are repeated.

Table V. Operational and structural parameters of the cell.

Parameter	Validation	Base case	Unit
Relative humidity (RH)	100[69]	100	%
Cell temperature (T)	80/60[69]	80	°C
Cell pressure (P)	1.0[69]	1.0	atm
Channel width (W_{ch})	1[69]	1	mm
Rib width (W_{rib})	1.5[69]	1.5	mm
GDL thickness (t_{GDL})	300[69]	300	μm
CL thickness (t_{CL})	15[69]	8	μm
PEM thickness (t_{PEM})	55[69]	55	μm
Pt/C mass ratio (γ_{PtC})	0.2[69]	0.4	–
Cathode platinum loading ($m_{\text{Pt,c}}$)	0.4[69]	0.25	mg cm^{-2}
Anode platinum loading ($m_{\text{Pt,a}}$)	0.1[69]	0.1	mg cm^{-2}
Cathode ionomer volume fraction ($\varepsilon_{\text{m,c}}$)	0.133[69]	0.2	–
Anode ionomer volume fraction($\varepsilon_{\text{m,a}}$)	0.133[69]	0.1	–
GDL porosity ($\varepsilon_{\text{void, GDL}}$)	0.8	0.8	–
Cathode charge transfer coefficient (α_{c})	1(80°C) 0.95(60°C)	1	–
Anode charge transfer coefficient (α_{a})	1	1	–
Cathode exchange current density ($i_{0,\text{c}}^{\text{ref}}$)	10^{-4}[68]	10^{-4}	A m^{-2}
Anode exchange current density ($i_{0,\text{a}}^{\text{ref}}$)	10^{4}[69]	10^{4}	A m^{-2}
Anode equilibrium potential (E_{a}^{eq})	0	0	V

Results and Discussion

Mathematical model validation.—To verify validity of the developed model, the simulated I-V curves are compared with the experimental ones adopted from[69] for a single cell with an active electrode area of $1 \times 1\ \text{cm}^2$. The mathematical model of Section Mathematical Modeling is solved using the values reported in Table V for two different cell temperatures. The values of these structural and operational parameters are according to those reported in[69] for the experimental condition. It is noteworthy to note that, similar to[69] where the experimental data was adopted from, the model in the present work is based on parallel straight channels. This results in mass transport within the catalyst layer being primarily driven by molecular diffusion rather than convection. Other flow channel configurations, such as serpentine or interdigitated designs, warrant further investigation, which lies beyond the scope of this

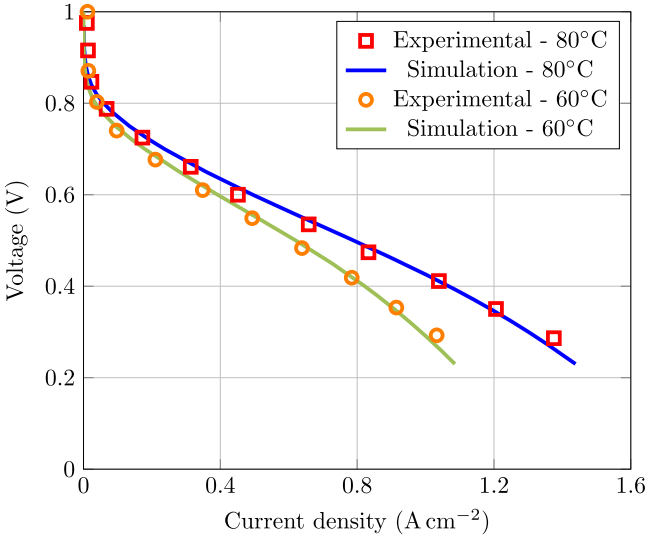

Figure 2. Validation of the simulation results against experimental ones.[69]

Table VI. Optimization scenarios.

Optimization scenario	Decision variable(s)	m_{Pt}^{max} (mg cm^{-2})	ε_l^{max}
OPT-I	ε_{PtC} and ε_l	0.25	0.2
OPT-II	ε_{PtC}	0.25	–
OPT-III	ε_l	–	0.2

study. The simulation and experimental curves are plotted in Fig. 2. Comparison of the experimental and simulated polarization curves reveals good agreement across different operating temperatures. At low current densities, a sharp decline could be observed in the cell voltage due to the activation losses. This overpotential is followed by Ohmic and concentration voltage drops at higher current densities. The former is caused by transport of electrons and protons through PtC and ionomer, which becomes considerable at medium current densities. The concentration overpotential, however, is dominant at high current density regions. The observed phenomenon is the result of slow transport of oxygen through the water and the ionomer films that surround the agglomerates. This sluggishness creates an oxygen delivery rate that is outpaced by the rate at which oxygen is consumed, leading to an imbalance in the cell performance. Furthermore, at high current densities, liquid water formation accelerates, leading to an excessive accumulation of liquid water in the CCL. This surplus of liquid water can block the pores that are responsible for oxygen delivery. This is included in the developed model by introducing an effective porosity. Figure 2 confirms that the present model well follows the polarization trend of a real PEMFC over a range of current densities and operating conditions.

Optimization of electrode structure.—This study focuses on the optimization of CCL structure at high current density levels. Under such working condition, the excess liquid water generated as a result of high electrochemical reaction rate blocks the pores. This makes the reactant delivery complicated and results in considerable oxygen depletion. Moreover, a thicker water film formed around the agglomerates at a relatively high current density increases the resistance against diffusion of oxygen into the agglomerate, where could react in the presence of platinum particles. Therefore, an optimal distribution of the constituents could enhance the utilization of available materials and provide a compromise between various transport and rate processes. The optimization is performed on a base case with a uniform material distribution. The parameters of this reference cell is reported in Table V. At a current density of 1.69 (A cm^{-2}) the base case corresponds to a voltage of 0.1 (V), which is computed by solving the governing equations. This is the operating point at which the optimization is conducted. Moreover, the generic form of the designated optimization problem in Eq. 41, considers two decision variables, including volume fractions of PtC and ionomer, as well as two global constraints. To extend the analysis scope of this study, various possible combinations of decision variables are considered in form of three different optimization scenarios as summarised in Table VI. As indicated in this table, scenario OPT-I represents the formulation of Eq. 41. This scenario includes simultaneous optimization of volume fractions of both PtC and ionomer. In this case, the average mass loading of platinum and volume fraction of ionomer are kept the same as the base case to obtain a fair comparison between the results. In scenario OPT-II, only the volume fraction of PtC is considered as the decision variable and the average platinum loading is restricted to that of the base case. In the final scenario (OPT-III), the volume fraction of the ionomer is the only decision variable and the average of this variable cannot exceed that of the base case.

Figure 3 demonstrates the optimization history of material distribution for OPT-I. The volume fractions of PtC, ionomer, and void (i.e., porosity) are shown at initial, intermediate, and optimized steps. Although the optimization process started with a uniform distribution of various phases, the optimal design shows a heterogeneous distribution of materials over the CCL domain. As can be seen in this figure, the optimized design solution exhibits high porosity in regions underneath the rib, while areas closer to the channel have relatively higher PtC and ionomer concentrations. This is because of the significant depletion of oxygen concentration in the regions farther away from the channel, specifically beneath the rib where oxygen delivery is insufficient. Closer examination of the optimal design depicted in Fig. 3 shows that the spatial distribution of materials remains uniform in the through-plane direction, which is attributed to the low thickness of CCL. Therefore, the optimization favors a heterogeneous distribution in lateral direction rather than through-plane direction. A similar behavior is observed in other optimization scenarios as well. Hence, for other cases, only the projected distributions on the lateral direction (y-direction) are plotted as shown in Fig. 4. According to the findings of this figure, materials distribution for various optimization scenarios is different. However, in any case, the optimal design shows a complicated heterogeneous material allocation, which provides a balance between different transport process and the electrochemical reaction. While the exact optimum solution depends on the cell characteristics and problem settings, analyzing the outcomes of Fig. 4 provides some useful qualitative information. What is striking about the optimized designs in this figure is that the porosity increases when getting farther from the channel. In the areas under the rib, oxygen concentration drops due to the sluggish mass transport. This causes a significant concentration overpotential. To overcome this problem, the optimization algorithm favors designs with higher porosity in those regions to compensate for the insufficient oxygen delivery through a higher effective diffusivity. Moreover, an increment in porosity might improve discharge of liquid water generated in those areas as a result of ORR. In addition, distribution of both PtC and ionomer have a local minimum in the middle of CCL, followed by symmetrical maxima close to the border of the regions under the channel and rib. Such a structure further facilitates dispersion of oxygen from areas under the channel, where oxygen concentration is relatively higher, and assures an improved proton transport and an escalated ECSA, where there is a potential for a higher reaction rate. The topologically-optimized distribution of PtC in our study shares similarities with the layout proposed by Havaej et al.[35] In their work, they achieved improved cell performance by employing a predefined parabolic distribution of catalyst material in the lateral direction. However, their approach relied on trial and error, searching for the optimal catalyst loading distribution through prescribed functions. In contrast, the present study introduces a novel optimization

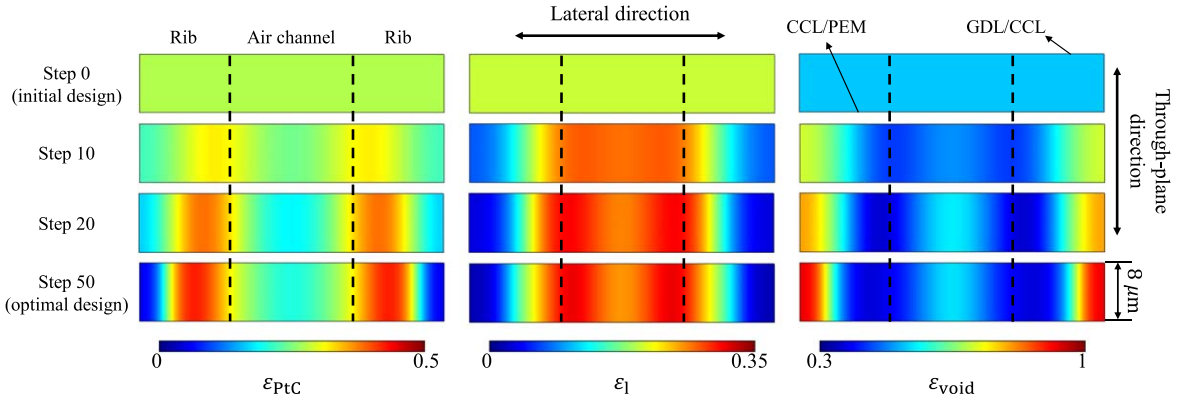

Figure 3. Optimization history of material distribution in CCL for scenario OPT-I (contour plots are not to scale).

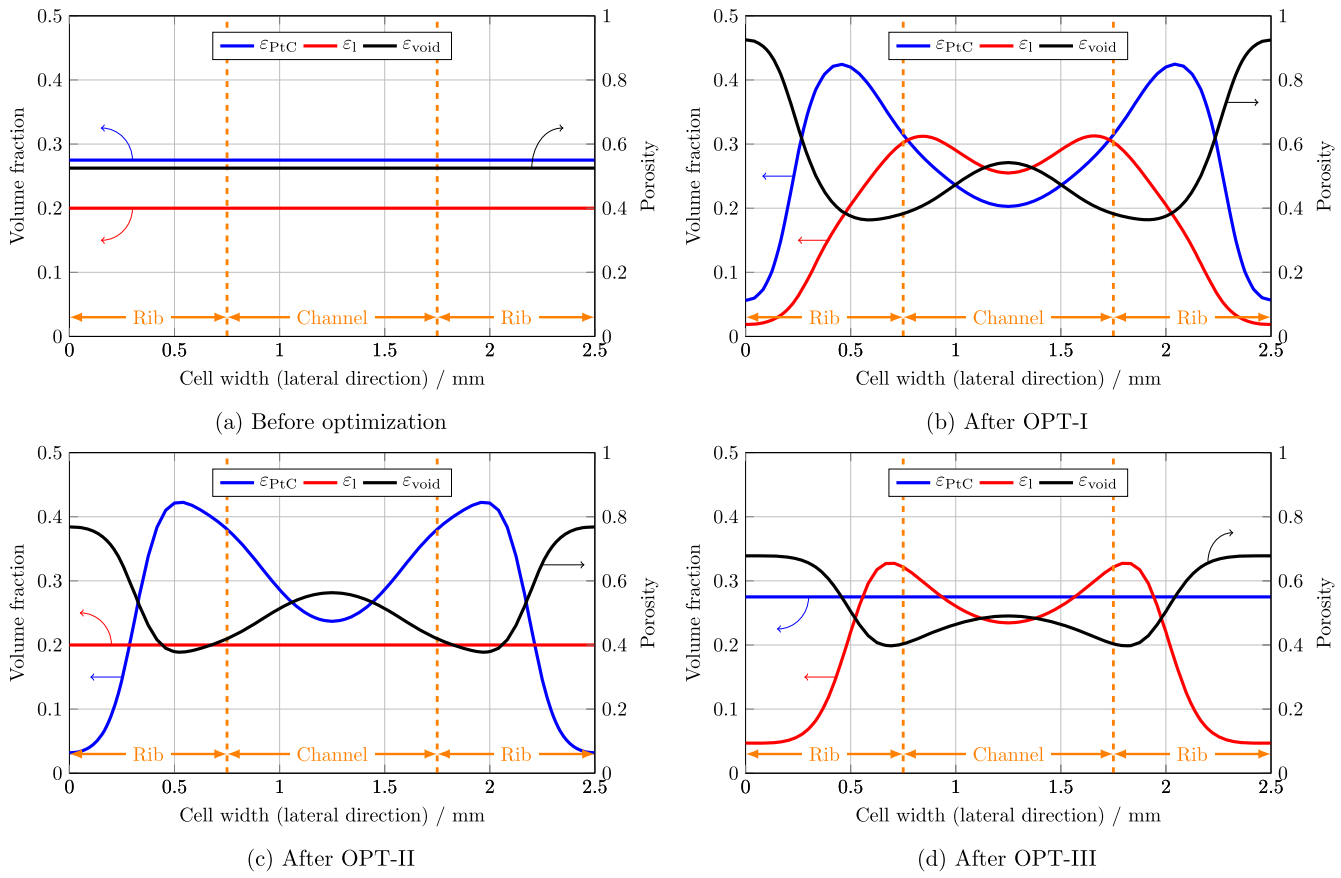

(a) Before optimization

(b) After OPT-I

(c) After OPT-II

(d) After OPT-III

Figure 4. Spatial distribution of constituents in lateral direction of CCL (a) before optimization, and after optimization with scenario (b) OPT-I, (c) OPT-II, and (d) OPT-III.

framework that offers a more robust and informed procedure for discovering such functionality. Our method does not depend on any prior information regarding the distribution and allows for a high degree of freedom to conduct multi-variable optimization. This advancement ensures greater accuracy and efficiency in identifying the best material distribution, ultimately leading to enhanced cell performance. Also of note is that achieving a finely graded design for CL in practice may not be possible at a high precision. Nevertheless, recent progress in additive manufacturing and 3D printing technologies has introduced new opportunities for realizing topologically optimized microstructures.[89–91]

Table VII compares the cell voltage (objective function) of optimized designs with that of the base case. The objective function increased between 18% and 42% after different optimization scenarios. From the data in this table, it is apparent that scenario OPT-I outperforms the two other ones thanks to its higher freedom in material arrangement provided by simultaneous optimization of two decision variables. While the cell voltage is enhanced

Table VII. Performance enhancement for various optimization scenarios.

Scenario	Base case	OPT-I	OPT-II	OPT-III
Cell voltage (V)	0.1	0.142	0.118	0.133
Voltage change (%)	–	42	18	33
Overpotential change (%)	–	−3.89	−1.67	−3.06
Activation	–	0.47	0.46	0.52
Ohmic	–	4.94	3.03	4.50
Concentration	–	−19.78	−9.89	−16.43

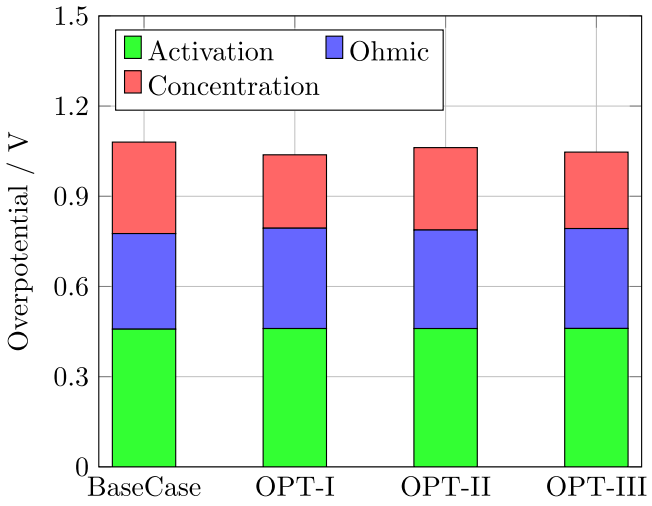

Figure 5. Overpotential breakdown analysis for various scenarios at current density of 1.69 (Acm^{-2}).

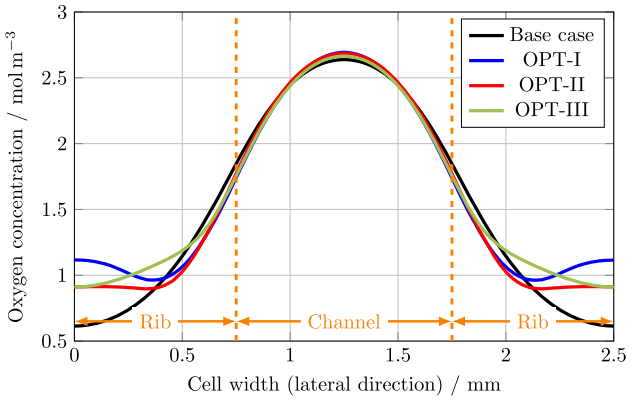

(a) Oxygen concentration distribution before and after optimization

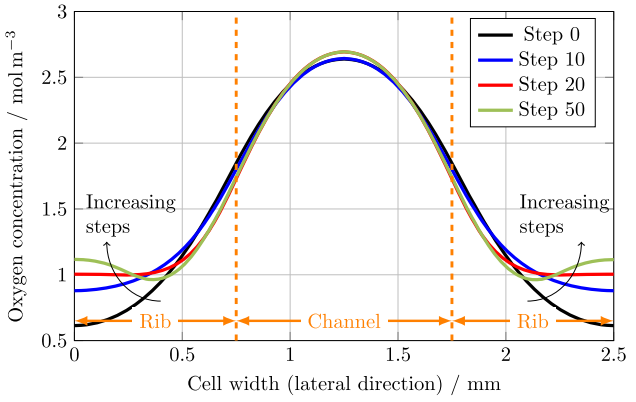

(b) Evolution of oxygen concentration distribution during optimization OPT-I

Figure 6. Spatial distribution of oxygen concentration: (a) compression of base case with three optimal designs and (b) optimization history for scenario OPT-I.

considerably in all optimizations, the overpotential improvement is relatively lower. However, it is anticipated that optimization of a 3D model, in which longitudinal effects are also included, may result in further enhancement. Evidently, such an optimization would require a significant amount of computational resources and it falls outside

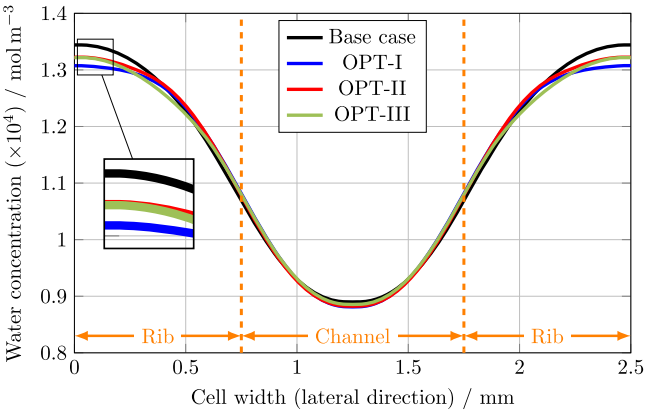

(a) Liquid water concentration

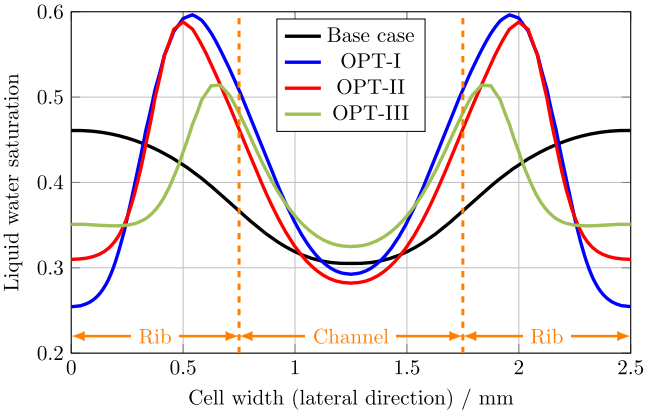

(b) Liquid water saturation

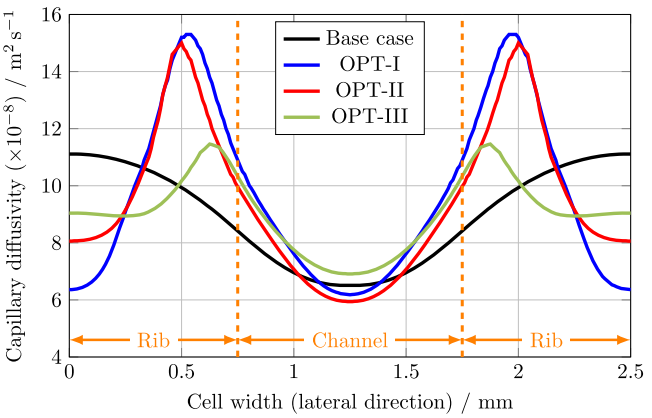

(c) Capillary diffusivity

Figure 7. Spatial distribution of (a) liquid water concentration, (b) liquid water saturation, and (c) capillary diffusivity before and after optimizations.

the scope of the present study. The total overpotential is decomposed using an applied-voltage breakdown (AVB) method proposed by Gerhardt et al.[92] which made it possible to separate contribution of each process quantitatively. Figure 5 provides an overview of total overpotential breakdown, including activation, ohmic, and concentration losses for different scenarios. Moreover, the changes of overpotential components with respect to the base case are given in Table VII. These findings suggest that, in all optimization scenarios, there is a slight increase in both activation and ohmic overpotentials. Despite these factors at play, the reduction in concentration overpotential ultimately proves to have the greatest impact on overall performance improvement.

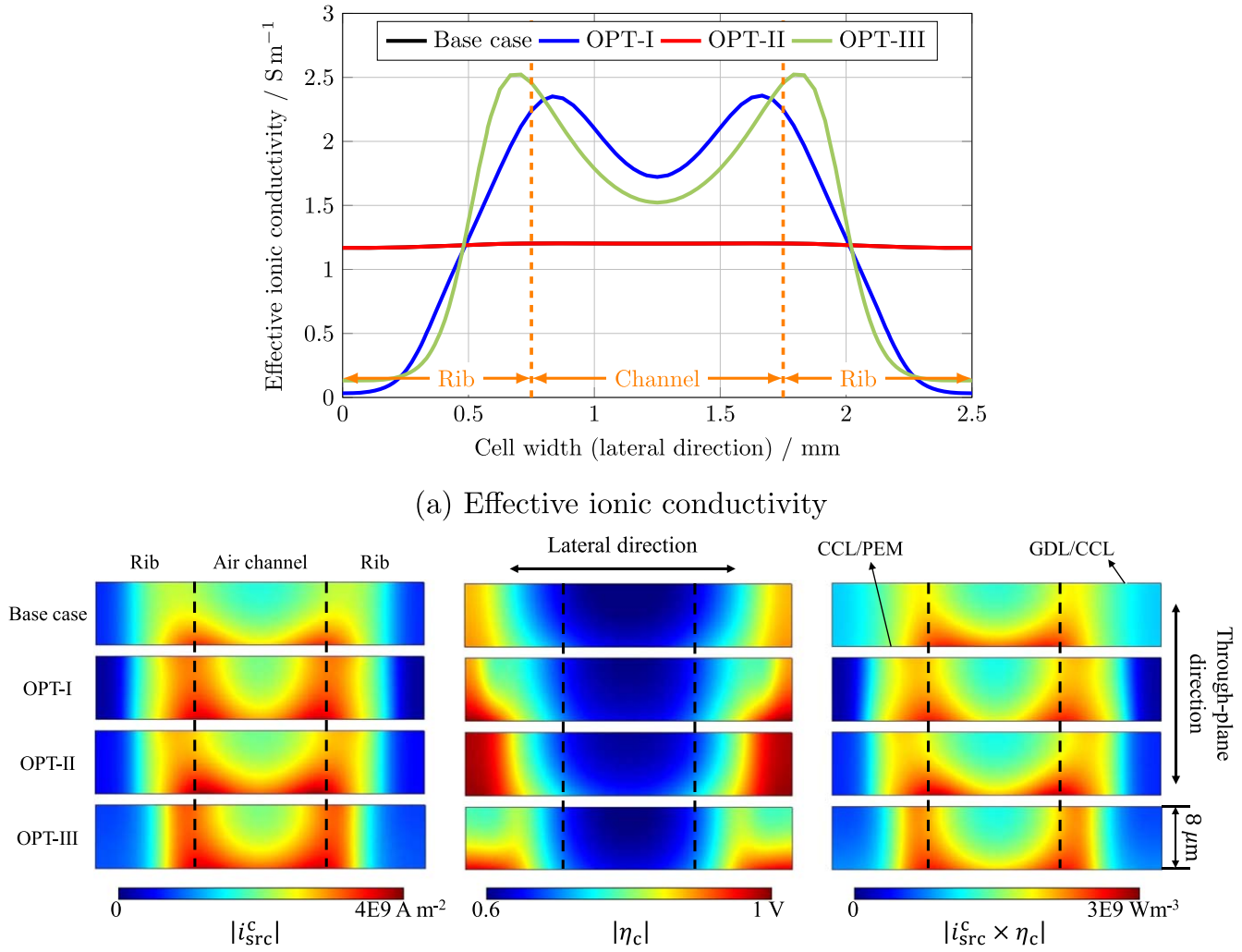

Figure 8. (a) Projected distribution of effective ionic conductivity and (b) distribution of current source and overpotential before and after optimizations.

According to the problem formulation of Eq. 41, the optimization algorithm favors those topological structures that maximize the cell voltage. This aim may be accomplished by obtaining a proper balance among transport and rate processes, such as oxygen diffusion, liquid water discharge, proton transport, and electrochemical reaction. To elucidate how an optimized design enhances the overall cell performance from a physical standpoint, some key parameters are inspected more in detail. To do so, first, the distributions of oxygen concentration are compared before and after optimization. Investigation of oxygen concentration shows that the gradient of this parameter along CL thickness (through-plane direction) is mainly negligible with a maximum difference of 10% in some limited parts. This variance is significantly smaller than that of lateral direction. Similar to what was mentioned before, the small thickness of CCL is the reason that makes the concentration gradient insignificant in this direction. Therefore, for the sake of clarity, the projected concentration along the cell width is presented in Fig. 6. As shown in Fig. 6a, all optimized designs have a higher average concentration compared to the base case. Significant improvements have been made, particularly in the concentration under the rib, which previously suffered from oxygen starvation in the base case. The observed increase in average concentration could be attributed to the more effective distribution of porosity, which augmented effective diffusivity in the areas under the rib. It could also be related to an enhanced product discharge which prevents pores blockage with the liquid water. This is discussed in a later part. Moreover, it can be clearly confirmed that such heterogeneous porosity distributions do not adversely affect the concentration in the rest of CCL, where the optimized porosity is lower than that of the uniform base case (see Fig. 4). Figure 6b illustrates the changes of concentration over the course of optimization OPT-I, as a representative scenario. According to this figure, at the initial step, the oxygen concentration shows a large drop in the lateral direction. As the optimization algorithm modifies the material distribution (see Fig. 3), it gradually compensates for oxygen depletion. In the final optimized design (step 50), the concentration at the two ends of CCL is almost two times higher than the initial uniform configuration. Interestingly, this significant improvement is achieved because of a better material distribution, despite the fact that the average porosity remains consistent in both the initial and final stages.

Water management is a critical issue in the design of low temperature PEMFCs since the water exists in the liquid phase. The liquid water accumulation increases the gas transport resistance in the secondary pores. Moreover, due to the hydrophilic nature of the ionomer, a greater amount of water results in a thicker liquid water film around the agglomerates. This, in turn, leads to an additional resistance against the delivery of oxygen to the platinum particles. Figure 7 compares distribution of water concentration, saturation, and capillary diffusivity before and after optimizations. According to Fig. 7a, the overall amount of accumulated water is

decreased in CCL after all optimizations. This decline is more significant in areas under the rib. As discussed before, the oxygen concentration is low in those areas due to the sluggish mass transport. A decrease in the liquid water accumulation may facilitate the oxygen delivery process. This has been already confirmed by inspection of oxygen concentration distribution (see Fig. 6). Liquid water saturation, that represents the ratio of water volume to void volume, is another critical index. Despite the decrease in local water concentration in the CCL after optimization, as depicted in Fig. 7b, the saturation exhibits a non-monotonic trend. Since saturation is related to both water volume and porosity, this behavior is attributed to the non-uniform porosity distribution after optimization. Optimization favored low porosity in certain areas, which, in turn, led to an increase in saturation within those regions. The capillary diffusivity is correlated to the water saturation through Leverett J-function. A higher saturation in some part of the CCL improved the capillary diffusivity in those areas as illustrated in Fig. 7c. This higher diffusivity is the reason behind the enhanced water management in optimized designs.

As previously mentioned, during the process of hydrogen oxidation in ACL, hydrogen ions (protons) are produced. These ions are then transported across a polymeric membrane to the CCL, where they participate in ORR. These protons are transported through the ionomer phase within CCL. Therefore, ionic conductivity of CCL is another crucial factor in determining the overall cell performance. The intrinsic ionic conductivity of the ionomer is much lower than the electric conductivity of PtC. Hence, electron transport is not a limiting phenomenon. The effective ionic conductivity depends on water content as well as volume fraction of ionomer. While excess water generation at high current densities can have negative impacts on oxygen delivery, it may have a positive effect on ionic conductivity. Since in this study it is assumed that the cell is working at a high current density and RH level, the ionomer is fully hydrated. In such a case, the ionomer volume fraction becomes the determining factor. The distribution of effective ionic conductivity is depicted in Fig. 8a. Because the ionomer distribution is kept unchanged during OPT-II, as expected, the conductivity plot of this scenario coincide that of the base case. The conductivity distribution after OPT-I and OPT-III follows the trend of the ionomer volume fraction distribution. A heterogeneous distribution of ionomer leads into a non-uniform conductivity. Although the ionic conductivity in the two ending parts far from the channel is reduced compared to the base case, it is considerably enhanced in the rest of CCL. The average effective conductivity throughout CCL is increased from a value of $1.19\ \mathrm{S\ m^{-1}}$ for the base case to $1.33\ \mathrm{S\ m^{-1}}$ and $1.32\ \mathrm{S\ m^{-1}}$ for OPT-I and OPT-III, respectively. This 11% enhancement is achieved thanks to an uneven ionomer distribution. According to Fig. 8b, which shows the distributions of current source, overpotential, and power loss, a higher reaction rate can be observed in the areas beneath rib/channel border before optimization. Also, in a through-plane direction, the regions close to the CCL/PEM interface show a higher potential for ORR. As a result, instead of distributing the ionomer phase uniformly, the optimization algorithm places more ionomer in areas with a high possibility for reaction. Increasing the ionic conductivity in regions where there is a high potential for reaction may further improve the conversion rate in those areas thanks to an improved proton transport. Thus, this variation in ionomer distribution made the ionic conductivity to match the reaction rate and consequently enhanced the material utilization. It is noteworthy that, since the optimization is performed at a constant current density, the average current density in all current source contour plots ($|i^{c}_{src}|$) are the same. However, its distribution is changed so that the overall performance is enhanced. Investigating the overpotential magnitude ($|\eta_c|$) presented in Fig. 8b shows a local increase in some parts of the CCL after optimization. However, this increase in overpotential is accompanied by a decrease in the current source in those regions as well. The combined effect of these two changes resulted in a lower power loss ($|i^{c}_{src} \times \eta_c|$) over the entire CCL that has been confirmed before through the overall cell performance. The power loss contour plots ($|i^{c}_{src} \times \eta_c|$) are compared for all scenarios in Fig. 8b. For instance, after OPT-I, the average power loss decreases by 8% compared to the base case, from an initial value of $1.59 \times 10^{9}\ \mathrm{W\ m^{-3}}$ to a final value of $1.46 \times 10^{9}\ \mathrm{W\ m^{-3}}$.

Conclusions

This research provides a mathematical optimization approach for the mathematically optimized design of material distribution in CL of PEMFC based on TO. First, a two-phase flow model of PEMFC is developed to simulate the cell performance. The model is validated against experimental data. Next, TO is employed to optimize the material distribution in CCL with the objective of increasing the cell performance. While a mathematical model is an essential part of any optimization, this work primarily focuses on applying TO to PEMFC, rather than on the model itself. The performance enhancement is formulated as a higher voltage at a given current density. The optimization is performed with various decision variables. Under a high working current density, the excess liquid water generated in CCL may cause significant mass transport losses. An optimal design can reduce the concentration overpotential through an improved distribution of materials within the electrode. In general, an optimal CL design showed a higher volume fraction of PtC and ionomer in areas under the channel compared to those under the rib. The optimization results are further investigated through the breakdown of overpotential contributions. It is confirmed that the concentration overpotential is considerably decreased after optimization. Moreover, inspecting the oxygen distribution in the CCL proves the improvement in oxygen delivery to those areas under the rib that suffer from oxygen starvation. This improvement in oxygen transport is achieved thanks to a better porosity distribution, which in return increases the effective gas diffusivity and enhances the liquid water discharge. A better ionomer placement in accordance to reaction rate also positively affected the cell performance. In the application of TO for electrode design, reliable design solutions require validating the models against experimental data to ensure real-world performance improvements. While existing models of PEMFC, including the present work, have been validated under varying operational conditions, their applicability to different structural designs remains uncertain. To enhance the robustness of TO applications for electrode design and ensure the practical relevance of the results, future PEMFC modeling efforts should prioritize validation across a wider range of structural conditions, which is currently less common compared to validation under operational conditions. Furthermore, continuum models must accurately capture the relationship between local microstructure and overall performance. In this regard, structural optimization based on alternative modeling approaches, such as the lattice Boltzmann method[93] or pore network modeling,[94] may offer valuable insights. Subsequent studies may explore the optimization of a 3D model, which is expected to provide additional benefits after introducing the effects of concentration depletion in longitudinal direction. However, solving a 3D multiphysics finite element model of a PEMFC at high current densities requires substantial computational resources. Furthermore, incorporating this into an optimization process, which involves repeated simulations, significantly increases the computational burden.

Acknowledgments

This work was supported by Grant-in-Aid for JSPS Fellows number 22KJ2198 and JSPS KAKENHI Grant number 21H04540. This research has also received funding support from King Mongkut's University of Technology Thonburi (KMUTT), Thailand Science Research and Innovation (TSRI), and National Science, Research and Innovation Fund (NSRF) Fiscal year 2024.

ORCID

Mehrzad Alizadeh https://orcid.org/0000-0001-5086-1683
Patcharawat Charoen-amornkitt https://orcid.org/0000-0001-6382-3715
Takahiro Suzuki https://orcid.org/0000-0002-1487-867X

References

1. Y. Matsui, M. Kawase, T. Suzuki, and S. Tsushima, "Electrochemical cell recharging by solvent separation and transfer processes." *Sci. Rep.*, **12**, 1 (2022).
2. N. Limjeerajarus and P. Charoen-Amornkitt, "Effect of different flow field designs and number of channels on performance of a small PEFC." *International Journal of Hydrogen Energy*, **40**, 7144 (2015).
3. T. Capurso, M. Stefanizzi, M. Torresi, and S. Camporeale, "Perspective of the role of hydrogen in the XXI century energy transition." *Energy Conversion and Management*, **251**, 114898 (2022).
4. J. St-Pierre, "Perspectiveoxygen-based fuel cell and reversible systems for heavy-duty motive and stationary applications." *J. Electrochem. Soc.*, **169**, 044506 (2022).
5. E. Pahon, D. Bouquain, D. Hissel, A. Rouet, and C. Vacquier, "Performance analysis of proton exchange membrane fuel cell in automotive applications." *Journal of Power Sources*, **510**, 230385 (2021).
6. G. Wang, Y. Yu, H. Liu, C. Gong, S. Wen, X. Wang, and Z. Tu, "Progress on design and development of polymer electrolyte membrane fuel cell systems for vehicle applications: a review." *Fuel Processing Technology*, **179**, 203 (2018).
7. B. M. Stühmeier, R. J. Schuster, L. Hartmann, S. Selve, H. A. El-Sayed, and H. A. Gasteiger, "Modification of the electrochemical surface oxide formation and the hydrogen oxidation activity of ruthenium by strong metal support interactions." *J. Electrochem. Soc.*, **169**, 034519 (2022).
8. X. Chen, J. Xu, C. Yang, Y. Fang, W. Li, Y. Zhang, Z. Wan, and X. Wang, "Thermodynamic and economic study of pemfc stack considering degradation characteristic." *Energy Conversion and Management*, **235**, 114016 (2021).
9. K. Talukdar, M. A. Ripan, T. Jahnke, P. Gazdzicki, T. Morawietz, and K. A. Friedrich, "Experimental and numerical study on catalyst layer of polymer electrolyte membrane fuel cell prepared with diverse drying methods." *Journal of Power Sources*, **461**, 228169 (2020).
10. O. B. Rizvandi and S. Yesilyurt, "A transient pseudo-3d model of the PEM fuel cell for the analysis of dead-ended anode and anode bleeding operation modes." *Electrochimica Acta*, **324**, 134866 (2019).
11. M. E. Abdelrahman, H. Zhang, G. Wu, X. Li, and S. Litster, "Half-cell electrode assessments of a crossover-tolerant direct methanol fuel cell with a platinum group metal-free cathode." *Electrochimica Acta*, **416**, 140262 (2022).
12. L. Osmieri and Q. Meyer, "Recent advances in integrating platinum group metal-free catalysts in proton exchange membrane fuel cells." *Current Opinion in Electrochemistry*, **31**, 100847 (2022).
13. X. Qu, Y. Li, G. Li, R. Ji, S. Yin, X. Cheng, C. Wang, J. Yang, Y. Jiang, and S. Sun, "Boosting the ORR performance of Fe-N/C catalyst via increasing the density and modifying the electronic structure of Fe-N_x active sites." *Electrochimica Acta*, **403**, 139604 (2022).
14. T. Reshetenko, G. Randolf, M. Odgaard, B. Zulevi, A. Serov, and A. Kulikovsky, "The effect of proton conductivity of Fe-N-C-based cathode on pem fuel cell performance." *J. Electrochem. Soc.*, **167**, 084501 (2020).
15. D. Banham, J. Y. Choi, T. Kishimoto, and S. Ye, "Integrating pgm-free catalysts into catalyst layers and proton exchange membrane fuel cell devices." *Adv. Mater.*, **31**, 1804846 (2019).
16. S. Stariha, K. Artyushkova, M. J. Workman, A. Serov, S. Mckinney, B. Halevi, and P. Atanassov, "PGM-free Fe-NC catalysts for oxygen reduction reaction: Catalyst layer design." *Journal of Power Sources*, **326**, 43 (2016).
17. L. Dunsmore, A. Uddin, H. Zhang, G. Wu, and S. Litster, "Non-planar platinum group metal-free fuel cell cathodes for enhanced oxygen transport and water rejection." *Journal of Power Sources*, **506**, 230188 (2021).
18. P. Charoen-amornkitt, T. Suzuki, and S. Tsushima, "Effects of voltage-dependence of the constant phase element and ohmic parameters in the modeling and simulation of cyclic voltammograms." *J. Electrochem. Soc.*, **167**, 166506 (2020).
19. P. Charoen-Amornkitt, T. Suzuki, and S. Tsushima, "Determination of constant phase element parameters under cyclic voltammetry conditions using a semi-theoretical equation." *Electrochemistry*, **87**, 204 (2019).
20. P. Charoen-amornkitt, T. Suzuki, and S. Tsushima, "Ohmic resistance and constant phase element effects on cyclic voltammograms using a combined model of mass transport and equivalent circuits." *Electrochimica Acta*, **258**, 433 (2017).
21. P. Charoen-amornkitt, W. Pholauyphon, T. Suzuki, and S. Tsushima, "An approach to unify capacitance measurements of electric double layer capacitors using sinusoidal potential scan." *Journal of Energy Storage*, **66**, 107522 (2023).
22. M. L. Perry, J. Newman, and E. J. Cairns, "Mass transport in gas-diffusion electrodes: a diagnostic tool for fuel-cell cathodes." *J. Electrochem. Soc.*, **145**, 5 (1998).
23. Q. Wang, M. Eikerling, D. Song, and Z. Liu, "Structure and performance of different types of agglomerates in cathode catalyst layers of PEM fuel cells." *Journal of Electroanalytical Chemistry*, **573**, 61 (2004).
24. M. Eikerling, "Water management in cathode catalyst layers of PEM fuel cells: a structure-based model." *J. Electrochem. Soc.*, **153**, E58 (2006).
25. M. Secanell, K. Karan, A. Suleman, and N. Djilali, "Multi-variable optimization of pemfc cathodes using an agglomerate model." *Electrochimica Acta*, **52**, 6318 (2007).
26. A. Kulikovsky, "The regimes of catalyst layer operation in a fuel cell." *Electrochimica Acta*, **55**, 6391 (2010).
27. K. O'Neil, J. P. Meyers, R. M. Darling, and M. L. Perry, "Oxygen gain analysis for proton exchange membrane fuel cells." *international Journal of Hydrogen Energy*, **37**, 373 (2012).
28. E. Sadeghi, A. Putz, and M. Eikerling, "Effects of ionomer coverage on agglomerate effectiveness in catalyst layers of polymer electrolyte fuel cells." *Journal of Solid State Electrochemistry*, **18**, 1271 (2014).
29. M. Sabharwal and M. Secanell, "Microstructural analysis of electrode performance in fuel cells at varying water contents." *ECS Trans.*, **86**, 51 (2018).
30. M. Moore, S. Shukla, S. Voss, K. Karan, A. Weber, I. Zenyuk, and M. Secanell, "A numerical study on the impact of cathode catalyst layer loading on the open circuit voltage in a proton exchange membrane fuel cell." *J. Electrochem. Soc.*, **168**, 044519 (2021).
31. M. Sabharwal and M. Secanell, "Understanding the effect of porosity and pore size distribution on low loading catalyst layers." *Electrochimica Acta*, **419**, 140410 (2022).
32. B. Prince Abraham and M. Kalidasa, "Influence of catalyst layer and gas diffusion layer porosity in proton exchange membrane fuel cell performance." *Electrochim Acta*, **389**, 138793 (2021).
33. P. He, Y. T. Mu, J. W. Park, and W. Q. Tao, "Modeling of the effects of cathode catalyst layer design parameters on performance of polymer electrolyte membrane fuel cell." *Applied Energy*, **277**, 115555 (2020).
34. E. Carcadea, M. Varlam, A. Marinoiu, M. Raceanu, M. Ismail, and D. Ingham, "Influence of catalyst structure on pem fuel cell performance-a numerical investigation." *International Journal of Hydrogen Energy*, **44**, 12829 (2019).
35. P. Havaej, M. Kermani, M. Abdollahzadeh, H. Heidary, and A. Moradi, "A numerical modeling study on the influence of catalyst loading distribution on the performance of polymer electrolyte membrane fuel cell." *International Journal of Hydrogen Energy*, **43**, 10031 (2018).
36. R. Friedmann and T. Van Nguyen, "Optimization of the microstructure of the cathode catalyst layer of a pemfc for two-phase flow." *J. Electrochem. Soc.*, **157**, B260 (2009).
37. M. Alizadeh and F. Torabi, "Precise pem fuel cell parameter extraction based on a self-consistent model and SCCSA optimization algorithm." *Energy Conversion and Management*, **229**, 113777 (2021).
38. J. Shen, L. Xu, H. Chang, Z. Tu, and S. H. Chan, "Partial flooding and its effect on the performance of a proton exchange membrane fuel cell." *Energy Conversion and Management*, **207**, 112537 (2020).
39. X. Wang and B. Zhou, "Liquid water flooding process in proton exchange membrane fuel cell cathode with straight parallel channels and porous layer." *Journal of Power Sources*, **196**, 1776 (2011).
40. O. Antoine, Y. Bultel, P. Ozil, and R. Durand, "Catalyst gradient for cathode active layer of proton exchange membrane fuel cell." *Electrochimica Acta*, **45**, 4493 (2000).
41. J. Liu and M. Eikerling, "Model of cathode catalyst layers for polymer electrolyte fuel cells: the role of porous structure and water accumulation." *Electrochimica Acta*, **53**, 4435 (2008).
42. W. Li, R. Lin, and Y. Yang, "Investigation on the reaction area of PEMFC at different position in multiple catalyst layer." *Electrochimica Acta*, **302**, 241 (2019).
43. G. Y. Chen, C. Wang, Y. J. Lei, J. Zhang, Z. Mao, Z. Q. Mao, J. W. Guo, J. Li, and M. Ouyang, "Gradient design of Pt/C ratio and nafion content in cathode catalyst layer of pemfcs." *International Journal of Hydrogen Energy*, **42**, 29960 (2017).
44. M. Srinivasarao, D. Bhattacharyya, and R. Rengaswamy, "Optimization studies of a polymer electrolyte membrane fuel cell with multiple catalyst layers." *Journal of Power Sources*, **206**, 197 (2012).
45. Q. Wang, M. Eikerling, D. Song, Z. Liu, T. Navessin, Z. Xie, and S. Holdcroft, "Functionally graded cathode catalyst layers for polymer electrolyte fuel cells: I. theoretical modeling." *J. Electrochem. Soc.*, **151**, A950 (2004).
46. Z. Xie, T. Navessin, K. Shi, R. Chow, Q. Wang, D. Song, B. Andreaus, M. Eikerling, Z. Liu, and S. Holdcroft, "Functionally graded cathode catalyst layers for polymer electrolyte fuel cells: II. Experimental study of the effect of nafion distribution." *J. Electrochem. Soc.*, **152**, A1171 (2005).
47. R. Fan, G. Chang, Y. Xu, and J. Xu, "Multi-objective optimization of graded catalyst layer to improve performance and current density uniformity of a PEMFC." *Energy*, **262**, 125580 (2023).
48. P. Charoen-amornkitt, M. Alizadeh, T. Suzuki, and S. Tsushima, "Topologically optimized anode catalyst layers of proton exchange membrane water electrolyzers." *ECS Trans.*, **111**, 87 (2023).
49. M. Alizadeh, P. Charoen-amornkitt, T. Suzuki, and S. Tsushima, "Mixed topology optimization: a self-guided boundary-independent approach for power sources." *Energy Conversion and Management*, **294**, 117567 (2023).
50. D. Yang, Y. Hao, B. Li, P. Ming, and C. Zhang, "Topology optimization design for the lightweight endplate of proton exchange membrane fuel cell stack clamped with bolts." *International Journal of Hydrogen Energy*, **47**, 9680 (2022).
51. M. Alizadeh, P. Charoen-Amornkitt, T. Suzuki, and S. Tsushima, "Structural topology optimization and irreversibility analysis in an electrochemical reaction-diffusion system." *AIP Conference Proceedings*, *The 12th International Conference on Mechanical Engineering* (AIP Publishing)**3086** (2024).
52. S. Mukherjee, D. Lu, B. Raghavan, P. Breitkopf, S. Dutta, M. Xiao, and W. Zhang, "Accelerating large-scale topology optimization: State-of-the-art and challenges." *Archives of Computational Methods in Engineering*, **28**, 4549 (2021).
53. M. Long, T. Suzuki, M. Alizadeh, S. Tsushima, and P. Charoen-amornkitt, "The influence of rib and porous reactor thickness on topologically optimized structure in reaction-diffusion systems." *2023 IEEE Transportation Electrification Conference and Expo, Asia-Pacific (ITEC Asia-Pacific). IEEE*p. 1 (2023).

54. M. P. Bendsœ, "Optimal shape design as a material distribution problem." *Structural Optimization*, **1**, 193 (1989).
55. J. Alexandersen and C. S. Andreasen, "A review of topology optimisation for fluid-based problems." *Fluids*, **5**, 29 (2020).
56. P. Charoen-amornkitt, M. Alizadeh, T. Suzuki, and S. Tsushima, "Entropy generation analysis during adjoint variable-based topology optimization of porous reaction-diffusion systems under various design dimensionalities." *International Journal of Heat and Mass Transfer*, **202**, 123725 (2023).
57. M. Alizadeh, P. Charoen-amornkitt, T. Suzuki, and S. Tsushima, "Investigation of transport-reaction dynamics and local/global entropy production in topology optimization of two-species reaction-diffusion systems." *Chemical Engineering Science*, **275**, 118739 (2023).
58. R. Behrou, A. Pizzolato, and A. Forner-Cuenca, "Topology optimization as a powerful tool to design advanced pemfcs flow fields." *International Journal of Heat and Mass Transfer*, **135**, 72 (2019).
59. C. H. Chen, K. Yaji, S. Yamasaki, S. Tsushima, and K. Fujita, "Computational design of flow fields for vanadium redox flow batteries via topology optimization." *Journal of Energy Storage*, **26**, 100990 (2019).
60. K. Yaji, S. Yamasaki, S. Tsushima, T. Suzuki, and K. Fujita, "Topology optimization for the design of flow fields in a redox flow battery." *Structural and Multidisciplinary Optimization*, **57**, 535 (2018).
61. F. Chen, J. Wang, and X. Yang, "Topology optimization design and numerical analysis on cold plates for lithium-ion battery thermal management." *International Journal of Heat and Mass Transfer*, **183**, 122087 (2022).
62. Z. Liu, X. Zeng, W. Zhao, Y. Gao, Y. Sun, and P. Yan, "A topology optimization design of three-dimensional cooling plate for the thermal homogeneity of lithium-ion batteries." *Energy Conversion and Management: X*, **14**, 100215 (2022).
63. V. A. Beck, J. J. Wong, C. F. Jekel, D. A. Tortorelli, S. E. Baker, E. B. Duoss, and M. A. Worsley, "Computational design of microarchitected porous electrodes for redox flow batteries." *Journal of Power Sources*, **512**, 230453 (2021).
64. C. Deng and W. Lu, "Geometry optimization of porous electrode for lithium-ion batteries." *ECS Trans.*, **97**, 249 (2020).
65. J. Lamb and P. Andrei, "Optimizing the composition of the pemfc catalyst layer." *ECS Trans.*, **98**, 67 (2020).
66. M. Alizadeh, P. Charoen-amornkitt, T. Suzuki, and S. Tsushima, "A numerical simulation of evolution processes and entropy generation for optimal architecture of an electrochemical reaction-diffusion system: comparison of two optimization strategies." *J. Electrochem. Soc.*, **170**, 114520 (2023).
67. O. Sigmund and K. Maute, "Topology optimization approaches." *Structural and Multidisciplinary Optimization*, **48**, 1031 (2013).
68. S. Li and B. Sundén, "Effects of gas diffusion layer deformation on the transport phenomena and performance of pem fuel cells with interdigitated flow fields." *International Journal of Hydrogen Energy*, **43**, 16279 (2018).
69. L. Xing, X. Liu, T. Alaje, R. Kumar, M. Mamlouk, and K. Scott, "A two-phase flow and non-isothermal agglomerate model for a proton exchange membrane (PEM) fuel cell." *Energy*, **73**, 618 (2014).
70. F. C. Cetinbas, S. G. Advani, and A. K. Prasad, "An improved agglomerate model for the PEM catalyst layer with accurate effective surface area calculation based on the sphere-packing approach." *J. Electrochem. Soc.*, **161**, F803 (2014).
71. B. K. Kanchan, P. Randive, and S. Pati, "Implications of non-uniform porosity distribution in gas diffusion layer on the performance of a high temperature PEM fuel cell." *International Journal of Hydrogen Energy*, **46**, 18571 (2021).
72. M. Moore, P. Wardlaw, P. Dobson, J. Boisvert, A. Putz, R. Spiteri, and M. Secanell, "Understanding the effect of kinetic and mass transport processes in cathode agglomerates." *J. Electrochem. Soc.*, **161**, E3125 (2014).
73. F. C. Cetinbas, S. G. Advani, and A. K. Prasad, "A modified agglomerate model with discrete catalyst particles for the PEM fuel cell catalyst layer." *J. Electrochem. Soc.*, **160**, F750 (2013).
74. W. Yoon and A. Z. Weber, "Modeling low-platinum-loading effects in fuel-cell catalyst layers." *J. Electrochem. Soc.*, **158**, B1007 (2011).
75. S. Kamarajugadda and S. Mazumder, "Numerical investigation of the effect of cathode catalyst layer structure and composition on polymer electrolyte membrane fuel cell performance." *Journal of Power Sources*, **183**, 629 (2008).
76. T. Suzuki, S. Okada, and S. Tsushima, "Analysis of ionomer distribution and Pt/C agglomerate size in catalyst layers by two-stage ion-beam processing." *J. Electrochem. Soc.*, **167**, 124513 (2020).
77. Y. T. Mu, P. He, Z. L. Gu, Z. G. Qu, and W. Q. Tao, "Modelling the reactive transport processes in different reconstructed agglomerates of a pefc catalyst layer." *Electrochimica Acta*, **404**, 139721 (2022).
78. K. Broka and P. Ekdunge, "Modelling the PEM fuel cell cathode." *Journal of Applied Electrochemistry*, **27**, 281 (1997).
79. F. Barbir, *PEM Fuel Cells: Theory and Practice* (Academic Press, USA) (2012).
80. H. Wu, P. Berg, and X. Li, "Modeling of PEMFC transients with finite-rate phase-transfer processes." *J. Electrochem. Soc.*, **157**, B1 (2009).
81. M. Sahraoui, Y. Bichioui, and K. Halouani, "Three-dimensional modeling of water transport in PEMFC." *International Journal of Hydrogen Energy*, **38**, 8524 (2013).
82. G. Zhang, J. Wu, Y. Wang, Y. Yin, and K. Jiao, "Investigation of current density spatial distribution in PEM fuel cells using a comprehensively validated multi-phase non-isothermal model." *International Journal of Heat and Mass Transfer*, **150**, 119294 (2020).
83. B. S. Lazarov and O. Sigmund, "Filters in topology optimization based on helmholtz-type differential equations." *International Journal for Numerical Methods in Engineering*, **86**, 765 (2011).
84. A. Kawamoto, T. Matsumori, S. Yamasaki, T. Nomura, T. Kondoh, and S. Nishiwaki, "Heaviside projection based topology optimization by a pde-filtered scalar function." *Structural and Multidisciplinary Optimization*, **44**, 19 (2011).
85. X. Huang and Y. Xie, "Convergent and mesh-independent solutions for the bi-directional evolutionary structural optimization method." *Finite Elements in Analysis and Design*, **43**, 1039 (2007).
86. J. V. Carstensen and J. K. Guest, "Projection-based two-phase minimum and maximum length scale control in topology optimization." *Structural and Multidisciplinary Optimization*, **58**, 1845 (2018).
87. C. Zillober, "A globally convergent version of the method of moving asymptotes." *Structural Optimization*, **6**, 166 (1993).
88. M. Bendsoe and O. Sigmund, *Topology Optimization: Theory, Methods, and Applications* (Springer Berlin Heidelberg, Germany) (2013).
89. M. D. R. Batista et al., "Design and additive manufacturing of optimized electrodes for energy storage applications." *Carbon*, **205**, 262 (2023).
90. V. Muñoz-Perales, M. van der Heijden, P. A. García-Salaberri, M. Vera, and A. Forner-Cuenca, "Engineering lung-inspired flow field geometries for electrochemical flow cells with stereolithography 3d printing." *ACS Sustainable Chemistry & Engineering*, **11**, 12243 (2023).
91. C. Lee, W. J. Kort-Kamp, H. Yu, D. A. Cullen, B. M. Patterson, T. A. Arman, S. Komini Babu, R. Mukundan, R. L. Borup, and J. S. Spendelow, "Grooved electrodes for high-power-density fuel cells." *Nat. Energy*, **8**, 685 (2023).
92. M. R. Gerhardt, L. M. Pant, J. C. Bui, A. R. Crothers, V. M. Ehlinger, J. C. Fornaciari, J. Liu, and A. Z. Weber, "Methodpractices and pitfalls in voltage breakdown analysis of electrochemical energy-conversion systems." *J. Electrochem. Soc.*, **168**, 074503 (2021).
93. Y. Su, "An improved weighted topology optimization lattice boltzmann model for porous structures of advection-diffusion chemical reaction systems." *Chemical Engineering Journal*, **495**, 153267 (2024).
94. M. Alizadeh, J. Gostick, T. Suzuki, and S. Tsushima, "Topological optimization for tailored designs of advection-diffusion-reaction porous reactors based on pore scale modeling and simulation: a PNM-NSGA framework." *Computers & Structures*, **301**, 107452 (2024).